remote sensing

Article

Classification of ALS Point Cloud with Improved Point Cloud Segmentation and Random Forests

Huan Ni [1], Xiangguo Lin [2] and Jixian Zhang [1,*]

[1] School of Resource and Environmental Sciences, Wuhan University, No. 129 Luoyu Road, Wuhan 430079, China; nih2015@yeah.net

[2] Chinese Academy of Surveying and Mapping, No. 28 Lianhuachixi Road, Beijing 100830, China; linxiangguo@gmail.com

[*] Correspondence: zhangjx@casm.ac.cn; Tel.: +86-10-6388-1816

Academic Editors: Bailang Yu, Lei Wang, Qiusheng Wu, Guoqing Zhou and Prasad S. Thenkabail
Received: 21 November 2016; Accepted: 14 March 2017; Published: 18 March 2017

Abstract: This paper presents an automated and effective framework for classifying airborne laser scanning (ALS) point clouds. The framework is composed of four stages: (i) step-wise point cloud segmentation, (ii) feature extraction, (iii) Random Forests (RF) based feature selection and classification, and (iv) post-processing. First, a step-wise point cloud segmentation method is proposed to extract three kinds of segments, including planar, smooth and rough surfaces. Second, a segment, rather than an individual point, is taken as the basic processing unit to extract features. Third, RF is employed to select features and classify these segments. Finally, semantic rules are employed to optimize the classification result. Three datasets provided by Open Topography are utilized to test the proposed method. Experiments show that our method achieves a superior classification result with an overall classification accuracy larger than 91.17%, and kappa coefficient larger than 83.79%.

Keywords: airborne laser scanning; point cloud segmentation; random forests; feature extraction; feature selection; semantic

1. Introduction

Commercial Airborne Laser Scanning (ALS) systems emerged in the mid-1990s for bathymetric and topographic applications. With the aid of direct geo-referencing technique, laser scanning equipment installed in the aircraft collect a cloud of laser range measurements for calculating the 3D coordinates (xyz) of the survey area [1]. In contrast to the 2D remote sensing imagery, an ALS point cloud is a swarm of points with XYZ coordinates [2], and thus describes the 3D topographic profiles of natural surfaces. Moreover, ALS point clouds have other benefits such as no effects of relief displacement, penetration of vegetation, and insensitivity to lighting conditions [1]. Therefore, ALS technique has been effectively used for ground point detection [3–7], topographic mapping [8], 3D city modelling [9–13], object recognition [14–16], solar energy estimation [17], etc.

Over the last two decades, significant contributions to the consolidation and extension of ALS data processing methods have been witnessed [1]. Among these processing methods, classifying the ALS data into categorical object instances is the first and most critical step for further data processing and model reconstruction [18]. Based on the granularity of basic processing units, these existing classification strategies can be categorized into three groups, i.e., point-based classification [18–20], segment-based classification [21–24], and multiple-entity-based classification [25]. A brief description of these existing methods is provided as follows.

1.1. Strategies for ALS Data Classification

1.1.1. Point-Based Classification

This kind of classification has attracted the most majority of research works in contrast to the other two kinds of classification strategies. In the process of point-based classification, ALS features of individual points [19] are firstly extracted. Then a classifier such as JointBoost [18] is trained using a number of selected training samples. Finally, the input ALS point cloud is classified via the trained classifier and the extracted features.

Additionally, to compute the features of individual points, a respective neighborhood definition is required to describe the local 3D structure around each individual point. Generally, there are three kinds of neighborhoods, i.e., spherical neighborhood [26], cylindrical neighborhood [27], and k-closest neighborhood [28]. Among the three neighborhoods, the scale parameter, either a fixed radius or a constant value k, is required. Due to the variation of local 3D structures and point densities, the constant scale parameter often fails to describe the local structural configurations. Thus, more and more studies such as [18,29–34] focus on seeking an optimal neighborhood size for each individual point. Unfortunately, these neighborhood optimization methods require repetitive calculations of eigenvectors and eigenvalues for each point, therefore they are rather time-consuming [35], which is the main disadvantage of this kind of classification.

1.1.2. Segment-Based Classification

Point cloud segmentation has been involved in ALS point cloud classification since its emergence. Generally, segment-based classification methods first perform segmentation on the point cloud after removing the ground points [21]. Then, the non-ground points are segmented into a number of segments, and features are extracted for each segment. Finally, a fuzzy model classifier [21,36] or several classification rules [22,24] are utilized to classify the segments. However, most of these studies are for non-ground points, and none of them uses Random Forests (RF) for feature selection and classification.

In addition, segment-based classification relies heavily on its employed segmentation method. A variety of point cloud segmentation methods have been proposed, which can be roughly classified as model-fitting-based methods, region-growing-based (RG-based) methods, and clustering-feature-based methods [37]. However, these existing methods segment input 3D point clouds into only one type of geometric structure. Actually, point clouds consist of a variety of geometric structures, such as planes, smooth surfaces and rough surfaces. In a complex 3D scene, there may exist regular and irregular man-made objects, and natural objects. Regular man-made objects such as buildings are composed of planar surfaces and smooth surfaces, while irregular man-made objects such as cars and natural objects like trees are composed of rough surfaces.

Therefore, segmenting point clouds into only one type of geometric structure is unreasonable. For example, existing planar segmentation methods segment all the points in an input point cloud into planes. If points are on building roofs, these methods are logical and perform well, however, if the points are on trees or cars, these methods which roughly segment these points into false planes are illogical. To obtain a superior classification result, we should consider a query point's geometric structure, and then segment it into a planar surface, smooth surface, or rough surface.

Although the aforementioned limitations exist, segment-based methods still have two main benefits in contrast to point-based classification methods, i.e., (i) segments are helpful to compute geometric features which relieve the dependence on neighborhood optimization [18,34] methods, and (ii) segments give several new attributes which are helpful to employ semantic rules.

1.1.3. Multiple-Entity-Based Classification

Multiple-entity-based classification [25] is considered as a combination of the segment-based and point-based classification. To solve the problem that a complex 3D scene is difficult to be characterized by only individual points or one kind of segments, this method utilizes three kinds of entities, i.e., points, planar segments, mean shift segments. In the process of classification, the input ALS point cloud is first divided into ground points and non-ground points. Next, planar segments are extracted from the non-ground points, and the scattered points are remained. Then, the planar segments are classified into several classes. The remained points are point-wise classified based on the contextual information offered by the classified planar segments. Finally, in complex areas where vegetation covers building roofs, mean shift segments are extracted to classify these areas.

However, the process of this method is a hierarchical classification procedure, which involves many steps. Besides, the mean shift segments and planar segments are derived from different segmentation methods, which adds additional classification steps. To simplify the classification process, a point cloud segmentation method that is able to extract more than one kind of segments is required.

These above three strategies have two common elements, including feature extraction and classifiers. Therefore, we present a brief description of both them as follows.

1.2. Feature Extraction

There are three main groups of features for ALS point cloud classification, i.e., reflectance-based features, descriptor-based features, and geometric features.

- The reflectance-based features are often related to the intensity [38] and echo [18] recorded by scanner systems. Therefore, the distinctiveness of this kind of features relies heavily on the quality of the scanner's signal.
- The descriptor-based features often employ spin images [39], shape distributions [40], histograms [41–43] to characterize a local 3D neighborhood. For all these descriptor-based features, a single object of the resulting feature vector is hardly interpretable [20].
- Common geometric features are height-based features [19], eigenvalue-based features [19,36], projection-area-based features [18,39], surface-based features [18], etc. Specifically, the eigenvalue-based features derived from the 3D structure tensor which is represented by the 3D covariance matrix derived from the 3D coordinates of all points within a local neighborhood, are discriminative in a variety of classification approaches. In contrast, the geometric features are deeply studied and widely used by state-of-the-art methods.

Most existing studies often compute as many features as possible to obtain a superior classification result. When a large number of features are extracted, some of them may be redundant. These redundant features not only increase the computational burden, but also waste the memory space. Therefore, recent studies introduce a feature selection procedure [19,20,38,44] as an additional step between feature extraction and classification steps.

1.3. Classifiers for ALS Data Classification

In the classification stage, many studies have tried locally independent classifiers, such as Support Vector Machine (SVM) [45], Adaptive Boosting (AdaBoost) [46], Expectation Maximum (EM) [47], RF [48,49], JointBoost [18], etc. The fundamental idea is to train a classifier by using given training samples which is used for prediction later [20]. Specifically, due to the excellent performance, the RF classifier [50] has received increasing attention [51]. Some studies [19,20,34,38] have looked into the potential of the RF classifier to improve urban objects classification and select uncorrelated features for ALS point clouds.

However, the integration of RF and the segment-based classification is rarely studied, as well as the importance analysis of segment features. In addition, the robustness of the classification methods is rarely analyzed when noises exist in the extracted features.

In this paper, we focus on the segment-based classification due to its advantages over the point-based classification. To address the aforementioned problems, we design a segment-based classification framework. This framework has three improvements compared to the existing methods:

(1) A novel point cloud segmentation method is proposed. This method clusters the points with regular neighborhoods into planar and smooth surfaces, and the points with scattered neighborhoods into rough surfaces.

(2) RF is integrated with the segment-based classification to select features and perform classification. The integration of RF and the segment-based classification improves the robustness of ALS point cloud classification.

(3) Semantic rules are employed to optimize the classification result. The semantic rules are more convenient to be detected when we process segments.

The outline of this paper is shown as follows. Section 2 presents the methodology of our proposed classification framework which contains a novel point cloud segmentation method, feature extraction based on segments, the integration of RF and segment-based classification, and post-processing based on semantic rules. The experiments and discussions are presented in Section 3, followed by Section 4 which summarizes the uncertainties, errors and accuracies of the proposed classification framework. The research conclusions are presented in Section 5.

2. Methodology

The proposed classification framework is composed of four stages as shown in Figure 1. First of all, a step-wise point cloud segmentation method which is able to cluster points with different neighborhoods into different geometric structures is proposed (see Section 2.1). Next, a segment rather than an individual point is considered as the basic processing unit for feature extraction (see Section 2.2). Then, we employ RF to select uncorrelated features based on a backward elimination method [52], and improve the robustness of ALS point clouds classification (see Section 2.3). Finally, we utilize semantic rules to optimize the classification result in the post-processing stage (see Section 2.4).

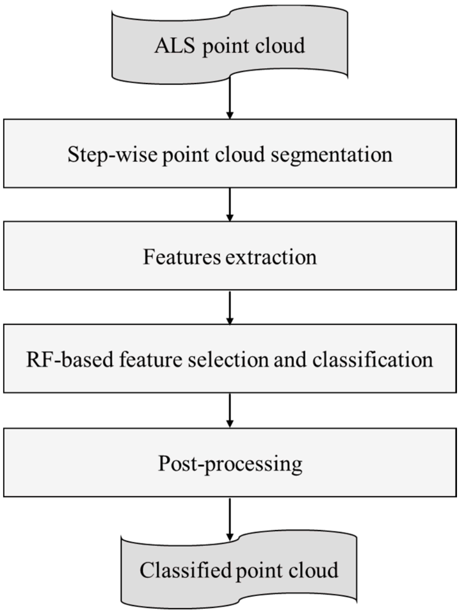
ALS point cloud
Step-wise point cloud segmentation
Features extraction
RF-based feature selection and classification
Post-processing
Classified point cloud

Figure 1. The proposed framework for airborne laser scanning (ALS) point cloud classification.

2.1. Step-Wise Point Cloud Segmentation

The proposed point cloud segmentation method is a RG-based one, and it clusters the points into planar surfaces, smooth surfaces, or rough surfaces.

Our segmentation procedure consists of three steps: region growing (RG) with RANdom SAmple Consensus (RANSAC), scattered points clustering, and small segments merging (see Figure 2). The first step extracts planar and smooth surfaces, and recognizes scattered points from the input point cloud. Then, the scattered points clustering step extracts rough surfaces from the scattered points. At last, an optional step is performed to merge small segments.

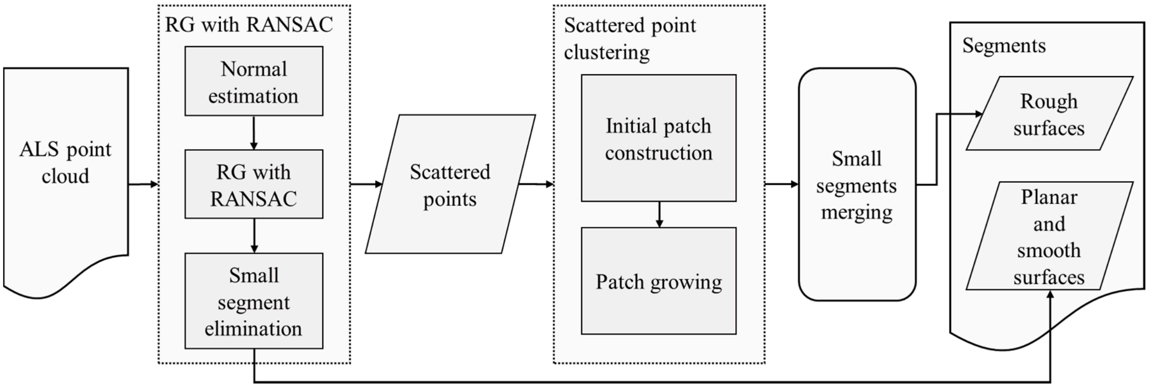

Figure 2. The flowchart of the step-wise point cloud segmentation.

It is notable that rough surfaces are separated from the other types of segments by the aforementioned steps. However, planar surfaces and smooth surfaces are not distinguished when we extract them in RG with RANSAC step. For the application of semantic recognition, planar surfaces and smooth surfaces are easily to be distinguished by their curvatures. In this study, the feature extraction, and the RF-based feature selection and classification stages perform without distinguishing these three types of segments.

2.1.1. RG with RANSAC

The plane-based RANSAC algorithm is widely used in point cloud segmentation tasks [53]. However, there is rare study employing RANSAC to improve RG-based segmentation methods.

To extract planar surfaces, two difficulties should be overcome for a RG-based method, i.e., non-optimal segmentations around edges where two surfaces meet [54], and the detection of small or narrow planes [55]. The integration of RANSAC and RG is able to solve both problems. In addition, we utilize a smooth RG procedure, which is able to extract smooth surfaces simultaneously.

There are three substeps in the RG with RANSAC step, i.e., normal estimation, RG with redefined constraints, and small segment elimination.

(1) Normal estimation

We employ RANSAC-Normal [56] to the RG-based method. Our previous approach [56] has validated that the RANSAC-Normal is efficient to extract a suitable plane from a complex neighborhood with intersecting surfaces. This procedure first determines the k_n neighbors of the i-th query point p_i, then fits a local plane based on the RANSAC algorithm, and finally, defines the normal of the fitted plane as the RANSAC-Normal.

In addition, during the normal estimation procedure, a number of scattered points are detected, and they are stored in a scattered point set SP. The pseudo code which shows details of this procedure, is presented in Algorithm 1. The parameter k_n is utilized to determine how many neighbors of a query point will be detected in Row 4. The parameter d_r is the threshold of the plane-based RANSAC algorithm, which is utilized in Row 5.

Algorithm 1. Normal estimation.

```
Input: Point cloud=$\{P\}$. Parameters: $k_n$, $d_r$
1: Regular point set $\{RP\} \leftarrow \varnothing$, Scattered point set $\{SP\} \leftarrow \varnothing$, Inlier Set $\{IN\} \leftarrow \varnothing$, Proportion Set $\{PR\} \leftarrow \varnothing$, Normal Set $\{NOR\} \leftarrow \varnothing$
2: For $i = 0$ to size ($\{P\}$) do
3:     Select i-th point $p_i$ as the query point
4:     Find $k_n$ neighbors for $p_i$ $NEI_i \leftarrow \mathcal{A}(i, k_n, P)$
5:     Determine the inliers using plane-based RANSAC algorithm $\{PI_i\} \leftarrow \mathcal{B}(NEI_i, d_r)$
6:     If $p_i \in \{PI_i\}$ then
7:         Compute proportion of $PI_i$ to $k_n$ neighbors $pr_i \leftarrow \mathcal{C}(N_i, d_r)$
8:         Normal estimation $nor_i \leftarrow \mathcal{D}(PI_i)$
9:         $\{RP\} \leftarrow \{RP\} \cup p_i$, $\{NOR\} \leftarrow \{NOR\} \cup nor_i$
10:    Else then
11:        $\{SP\} \leftarrow \{SP\} \cup p_i$
12:    End If
13:    $\{IN\} \leftarrow \{IN\} \cup PI_i$, $\{PR\} \leftarrow \{PR\} \cup pr_i$
14: End For
Output: $\{NOR\}$, $\{IN\}$, $\{PR\}$, $\{SP\}$, $\{RP\}$
```

Specifically, when plane-based RANSAC algorithm fits a local plane, it divides k_n neighbors into inliers PI_i and outliers (Row 5). The points in PI_i are on the fitted plane. If the query point p_i is in PI_i, we compute a proportion pr_i of the inliers PI_i to the k_n neighbors (Row 7).

Five sets (NOR, IN, PR, SP, RP) are generated in Algorithm 1, and they are useful for the RG with redefined constraints.

(2) RG with redefined constraints

This procedure is similar to the RG method presented in [57]. However, two constraints (local connectivity and surface smoothness [57]) are redefined based on the plane-based RANSAC algorithm.

- Constraint 1: local connectivity

  The points in a segment should be locally connected. In contrast to literature [57], we utilize the inliers IN_i to optimize this constraint. If p_i is in IN_i, the points in IN_i are local connective to it. Otherwise, there is no point local connective to p_i.

- Constraint 2: surface smoothness

  The points in a segment should locally make a smooth surface, whose RANSAC-Normals do not vary "too much" from each other. This constraint is expressed through dot product between normals:

$$||nor_s \cdot nor_n|| < th_\theta, \quad (1)$$

  where th_θ is the threshold of the constraint, nor_s is the normal of current seed, and nor_n is the normal of a point which is local connective to the current seed.

The pseudo code which shows details of the RG with redefined constraints procedure, is presented in Algorithm 2. The parameter th_θ is utilized to restrict the dot product between normals in the Row 12 and its usage is presented in Formula (1).

Algorithm 2. RG with redefined constraints.

```
Input: $\{RP\}$, $\{NOR\}$, $\{IN\}$, $\{PR\}$. Parameters: $th_\theta$
1: Available point list $\{A\} \leftarrow \{1, \ldots, \text{size}(RP)\}$
2: While $\{A\}$ is not empty do
3:     Current segment (planar or smooth face) $\{FC\} \leftarrow \varnothing$, Current seeds $\{SC\} \leftarrow \varnothing$
4:     Find a point in $\{RP\}$ with maximum $pr_i$ $p_{max} \leftarrow \mathcal{E}(RP, PR, i)$
5:     $\{SC\} \leftarrow \{SC\} \cup p_{max}$, $\{FC\} \leftarrow \{FC\} \cup p_{max}$, $\{A\} \leftarrow \{A\} \backslash i$
6:     For j=0 to size($\{SC\}$) do
7:        Set j-th point in $\{SC\}$ as current seed $SC_j$
8:        Find Current inliers of $SC_j$ $\left\{IN_j\right\} \leftarrow \{IN\}$        (constraint 1)
9:        For k=0 to size($IN_j$) do
10:           Neighbor point index $pn_k \leftarrow \left\{IN_j\right\}(k)$
11:           Compute $\cos\theta \leftarrow \Lambda\left(NOR\left\{SC_j\right\}, NOR\{pn_k\}\right)$
12:           if $\{A\}$ contains $pn_k$ and $\cos\theta < th_\theta$ then        (constraint 2)
13:              $\{FC\} \leftarrow \{FC\} \cup pn_k$, $\{A\} \leftarrow \{A\} \backslash pn_k$, $\{SC\} \leftarrow \{SC\} \cup pn_k$
14:           End If
15        End For
16:    End For
17:    $\{FP\} \leftarrow \{FP\} \cup \{FC\}$
18: End While
Output: Planar and smooth surfaces $\{FP\}$
```

Specifically, the constraint 1 is utilized in Row 8, and the constraint 2 is utilized in Row 12 of Algorithm 2.

(3) Small segment elimination

If the point density of trees is dense, there may be some small segments (planar and smooth surfaces) in the tree areas. Therefore, we should remove these small segments from FP, and add the points in these small segments to SP. There is a parameter in this procedure, i.e., the minimum size threshold s_{min}. s_{min} is expressed via the number of points in a segment.

Specifically, The RG with RANSAC step divides the input 3D point cloud into two point sets. The first set is the regular point set RP, and the second set is the scattered point set SP. Points in RP are clustered into planar and smooth surfaces, and points in SP are clustered into rough surfaces in the subsequent step. In the RG with RANSAC step, there are two procedures for dividing regular points and scattered points, which are shown as follows:

- For a query point p_i in Algorithm 1, we first find k_n neighbors of it, and then plane-based RANSAC is performed to determine inliers PI_i which is on the local fitted plane. If p_i is not in PI_i, it will be recognized as a scattered point.
- When the Algorithm 2 is performed, regular points are recognized and clustered into a number of segments containing planar and smooth surfaces. There may be misjudgment if a planar or smooth surface is small enough. Therefore, the small segment should be removed and points in it will be recognized as scattered points.

The result of the RG with RANSAC step is presented in Figure 3a. Points rendered in black are scattered points and other points are regular points.

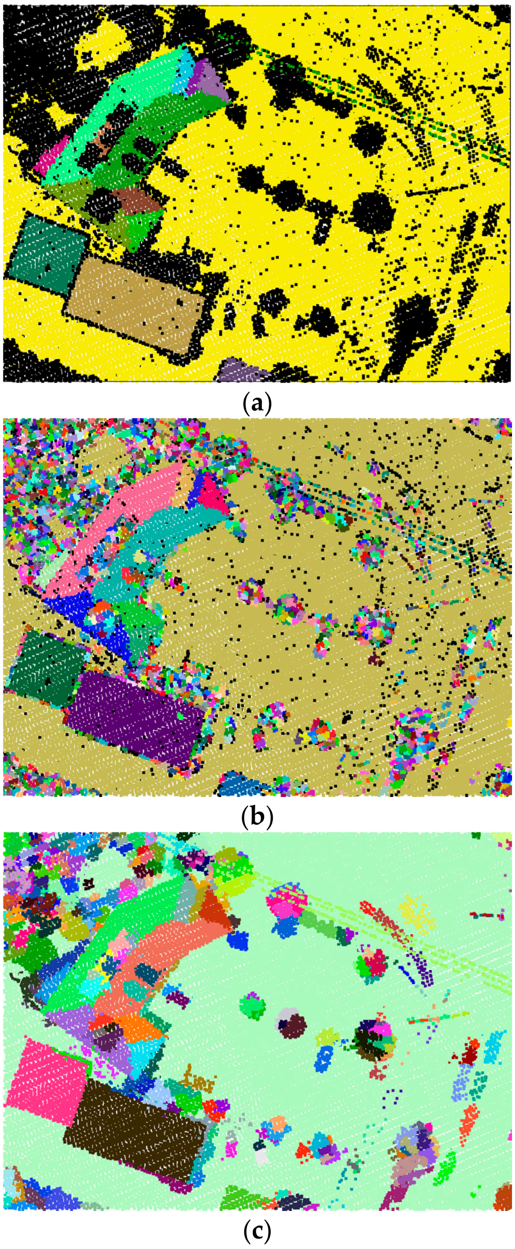
(**a**)

(**b**)

(**c**)

Figure 3. Results of internal steps in the step-wise point cloud segmentation: (**a**) Intermediate result after the process of the region growing (RG) with RANdom SAmple Consensus (RANSAC) step. The scattered points are rendered in black; (**b**) Intermediate result after the process of the initial patch construction; (**c**) The result of the step-wise point cloud segmentation.

2.1.2. Scattered Points Clustering

In this step, the scattered points in SP are first clustered into a number of initial patches, and then rough surfaces are extracted by growing these initial patches. The two substeps are detailed as follows:

(1) Initial patch construction

This substep is an iterative procedure. An initial patch is iteratively extracted from the scattered point set SP, until all the points in SP have been traversed. There are two parameters in this procedure, i.e., the maximum size threshold k_p and the maximum distance threshold d_{max}.

The number of points in an initial patch has to be smaller than k_p. Moreover, an initial patch has to satisfy the follow constraint:

$$\max_i[(x_i - x_c)^2 + (y_i - y_c)^2 + (z_i - z_c)^2] < d_{max} \text{ for } i = 1, \ldots, k_p. \tag{2}$$

where (x_i, y_i, z_i) is a point in an initial patch, and (x_c, y_c, z_c) is the centroid point of the initial patch. The details of this procedure is shown in Algorithm 3. To stabilize this procedure, the curvature of each point in $\{SP\}$ is estimated. These points in $\{SP\}$ are sorted according to their curvatures from minimum to maximum, and then are traversed in order.

Algorithm 3. Initial patch construction.

```
Input: Scattered point set $\{SP\}$. Parameters: $k_p$, $d_{max}$
1: Initial patch set $\{PT\} \leftarrow \varnothing$, Dirty indicator $\{DI\} \leftarrow$ false, Covariance matrix set $\{CM\} \leftarrow \varnothing$
2: Estimate curvatures of the points in $\{SP\}$ $\{CUR\} \leftarrow \mathfrak{A}(k_p)$
3: Sort $\{CUR\}$ from minimum to maximum, and obtain the sorted ID $\{IDs\}$ of each scattered point
4: For $i = 0$ to size $(\{IDs\})$ do
5:    Select i-th point $p_i$ as the query point
6:    Find $k_p$ nearest neighbors for $p_i$ based on a kd-tree $\{NEI_i\} \leftarrow \mathfrak{B}(i, k_p, \{SP\})$
7:    Extract a subset of the $k_p$ nearest neighbors based on the threshold $d_{max}$ $\{PT_i\} \leftarrow \mathfrak{C}(\{NEI_i\}, d_{max})$
8:    For $j = 0$ to size$(\{PT_i\})$ do
9:        If $DI(\{PT_i\}(j)) ==$ true
10:           Go to Row 4
11:       End If
12:   End For
13:   $\{PT\} \leftarrow \{PT\} \cup \{PT_i\}$
14:   Update $\{DI\}$ for all the points in $\{PT_i\}$ $\{DI\} \leftarrow \mathfrak{D}(\{DI\}, \{PT_i\})$
15: End For
16: Merge non-dirty points to their nearest patch $\{PT\} \leftarrow \mathfrak{E}(\{PT\}, \{DI\}, d_{max})$
17: Compute covariance matrix for each $\{PT_i\}$ in $\{PT\}$ $\{CM\} \leftarrow \mathfrak{F}(\{PT\})$
18: Sort initial patches based on their determinants with descending order $\{PT\} \leftarrow \mathfrak{G}(PT, CM)$
19: Normalize covariance matrices $\{CM\} \leftarrow \mathfrak{H}(CM)$
Output: $\{PT\}$, $\{CM\}$
```

As shown in Algorithm 3, the parameter k_p is utilized in Row 2 and 6 to determine how many neighbors of a query point will be detected for *kd*_tree search. The parameter d_{max} is utilized in Row 7 to restrict the distance between a neighbor and the query point. Only neighbors with the distance smaller than d_{max} are extracted to construct an initial patch. After all the initial patches are extracted, their covariance matrices are computed (Row 17). Let $p_i = (x_i, y_i, z_i)$ for $i = 1, 2, \ldots, N$, be the points in an initial patch, the covariance matrix M is defined as:

$$M = \frac{1}{N-1} \textstyle\sum_{i=1}^{N} (p_i - p_u)(p_i - p_u)^T, \tag{3}$$

where p_u is the mean vector of all the points in the patch.

After all the covariance matrices are determined, these initial patches in PT are sorted by the determinants of their covariance matrices. Finally, each covariance matrix is normalized by its determinant. The result of the initial patch construction is shown in Figure 3b.

(2) Patch growing

The patch growing is similar to the RG with redefined constraints procedure. Therefore, we do not present the pseudo code in the following. In this procedure, the growing unit is an initial patch rather than an individual point. Each initial patch is considered as a seed and grew in the order obtained in the initial patch construction procedure (Row 18 of Algorithm 3). Two constraints for patch growing are defined as follows:

- Constraint 1: local connectivity

  Only adjacent patches of the seed patch can be added into the current segment.

- Constraint 2: geometrical similarity

The geometrical difference D_{pa} of two patches in a segment has to be smaller than a threshold th_{sp}. D_{pa} is defined by using log Euclidean Riemannian metric [58] which measures how close two covariance matrices are. Given two covariance matrices M_1 and M_2, D_{pa} is computed as follows:

$$\boldsymbol{D_{pa}} = ||\log M_1 - \log M_2||_F, \tag{4}$$

where $\log(\cdot)$ is the matrix logarithm operator and $||\cdot||_F$ is the Frobenius norm.

After these two steps have been performed, points are clustered into three kinds of segments, i.e., planar, smooth, and rough surfaces. If small segments with a size smaller than the minimum size threshold s_{min} still exist, we merge them with their nearest neighbor segments. This step, which is an optimizing procedure, will iterate until all the segments are traversed. The result of the step-wise point cloud segmentation method is shown in Figure 3c.

2.2. Employed Features and Their Calculation

The difference of our method from the others is that we extract features of segments rather than individual points. Herein, we focus on four groups of geometric features, namely projection-area-based ones [18], eigenvalue-based ones [19], elevation-based ones [18], and other ones.

2.2.1. Projection-Area-Based Features

Projection-area-based features are first proposed in [39], and then are applied to 3D point cloud classification [18]. In this paper, we borrow the idea from literature [18] which is shown in Figure 4. However, the difference of our method is that the basic processing unit is a segment rather than an individual point. A segment has no fixed size compared to the neighborhood of an individual point. Therefore, a larger segment has larger projection area than a smaller segment. This problem affects the distinctiveness of this kind of features. We define two ratios to overcome this problem. The first one is the tangent plane projection ratio PR_t, and the second one is the horizontal projection ratio PR_h.

- Tangent plane projection ratio PR_t

  First of all, a covariance matrix is computed from all points in a segment. The normal vector is determined via the eigenvector corresponding to the lowest eigenvalue and a new 2D coordinate system with two coordinate axis corresponding to the largest and middle eigenvectors is constructed. Next, we project all the points in the segment along the normal direction into the coordinate system. The maximum and minimum coordinates in the coordinate system are determined, and a 2D grid is constructed by a given gird bin size. Then, we determine the number of non-bare bins that have projection points as the tangent plane projection area PA_t. Finally, the ratio PR_t is defined as:

$$PR_t = \frac{PA_t}{PAA_t}, \tag{5}$$

  where PAA_t is the number of all bins in the 2D grid.

- Horizontal projection ratio PR_h

This feature extraction procedure is similar to that of the tangent plane projection ratio, but we select the direction parallel to the Z-axis as the normal direction. Next, we construct 2D grid in XY-plane, and then accumulate the number of non-bare bins as the horizontal projection area PA_h. Finally, the ratio PR_h is defined as $PR_h = PA_h/PAA_h$, where PAA_h is the number of all bins. Figure 5a depicts this feature. In this paper, the bin size is set to 0.2 m for both the two projection-area-based features.

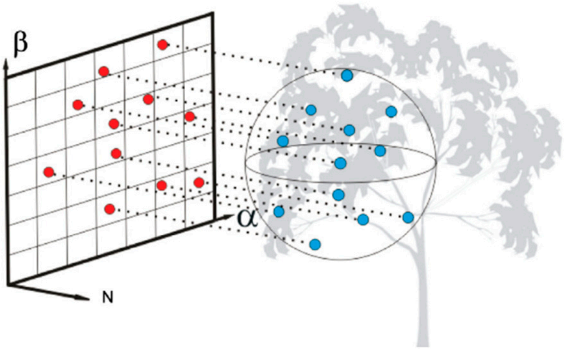

Figure 4. The calculation method of projection area [18].

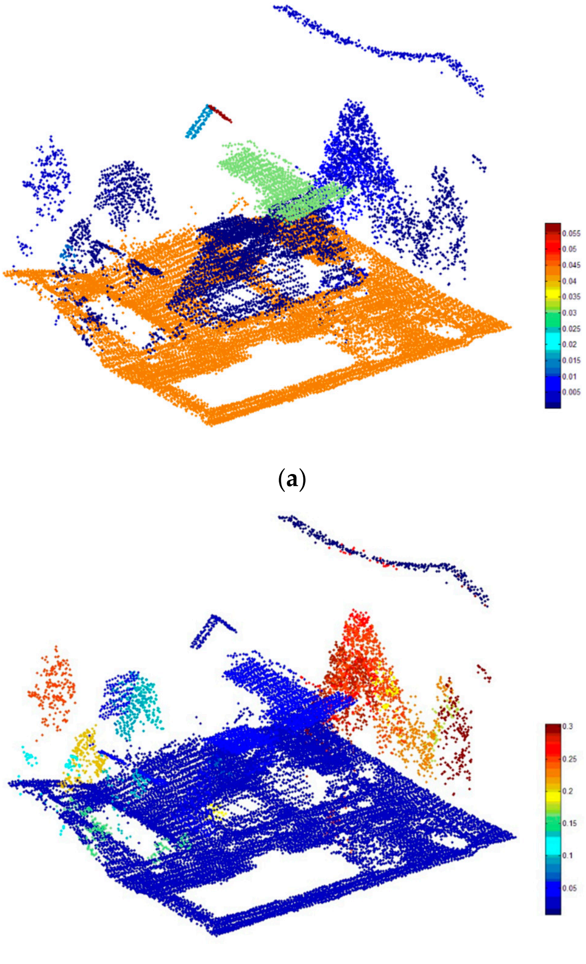

(**a**)

(**b**)

Figure 5. *Cont.*

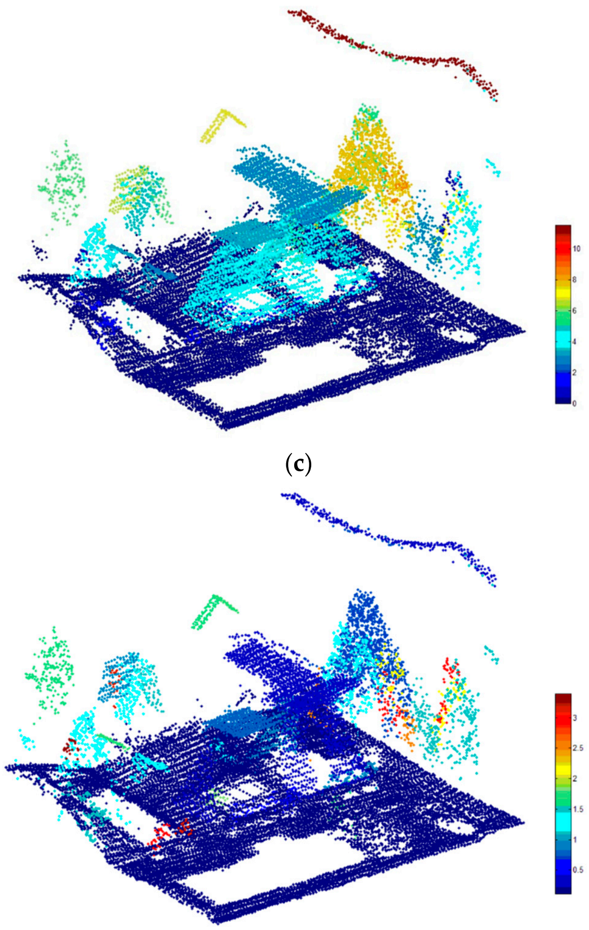

(**c**)

(**d**)

Figure 5. Segment-based features for 3D-point clouds classification, (**a**) horizontal projection area ratio PR_h; (**b**) eigenentropy λ_e; (**c**) relative elevation H_r; (d) slope O_{sl}.

2.2.2. Eigenvalue-Based Features

Herein, the covariance matrix is first determined by a segment, and then a set of positive eigenvalues $\lambda_1, \lambda_2, \lambda_3 (\lambda_1 > \lambda_2 > \lambda_3)$ [19] and normalized eigenvalues $e_i = \lambda_i / \sum_\lambda$ with $i \in \{1,2,3\}$ are computed. We employ ten eigenvalue-based features: highest eigenvalue λ_1, medium eigenvalue λ_2, lowest eigenvalue λ_3, linearity λ_l, planarity λ_p, scattering λ_s, anisotropy λ_a, omnivariance λ_o, eigenentropy λ_e (see Figure 5b) and change of curvature λ_c. The latter seven features are computed as:

$$\lambda_l = \frac{\sqrt{\lambda_1} - \sqrt{\lambda_2}}{\lambda_1}, \tag{6}$$

$$\lambda_p = \frac{\sqrt{\lambda_2} - \sqrt{\lambda_3}}{\lambda_1}, \tag{7}$$

$$\lambda_s = \frac{\sqrt{\lambda_3}}{\lambda_1}, \tag{8}$$

$$\lambda_a = \frac{e_1 - e_3}{e_1}, \tag{9}$$

$$\lambda_o = \sqrt[3]{e_1 e_2 e_3} \tag{10}$$

$$\lambda_e = -\sum_{i=1}^{3} e_i \ln(e_i), \tag{11}$$

$$\lambda_c = \frac{e_3}{e_1 + e_2 + e_3}. \tag{12}$$

2.2.3. Elevation-Based Features

In this part, we define four elevation-based features, the latter three borrow the idea from the height-based features for individual points presented in [18].

- Relative elevation H_r

  We first determine the adjacent segments for a query segment S_q in the XY-plane. Neighbors of all the points in S_q are searched in XY-plane by a *kd*_tree with a given distance threshold. The segments S_a^i for $i = 1, \ldots, N$ which contain the searched neighbors are the adjacent segments of S_q. Next, a point p_a^i which is closest to S_q is determined in S_a^i. Then, a point p_q^i which is closest to S_a^i is determined in S_q, and p_a^i and p_q^i construct a neighboring point pair which represents the relationship between S_a^i and S_q. Finally, the relative elevation H_r is defined as:

$$H_r = \max\left(Z\left(p_q^i\right) - Z\left(p_a^i\right)\right) \text{ for } i = 1, \ldots, N \tag{13}$$

  where $Z\left(p_q^i\right)$ is the z-coordinate of p_q^i, and $Z\left(p_a^i\right)$ is the z-coordinate of p_a^i. H_r is shown in Figure 5c.

- Elevation variance H_v

  This feature H_v is the variance of elevation values of all points in each segment. H_v is computed as:

$$H_v = \frac{1}{N}\sum_{i=1}^{N}\left(H_i - H_{ave}\right)^2, i = 1, \ldots, N, \tag{14}$$

  where N is the total number of points in the segment, H_{ave} is the average elevation of all points in the segment, H_i is the elevation of the i-th point in the segment.

- Elevation difference H_{diff}

  This feature is the difference between the highest elevation $H_{highest}$ and the lowest elevation H_{lowest} of a segment. In other words, the elevation difference H_{diff} is computed as $H_{diff} = H_{highest} - H_{lowest}$.

- Normalized elevation H_n

  This feature is the elevation difference between the centroid point and the lowest point of a segment. The normalized elevation H_n is defined as:

$$H_n = H_{ave} - H_{lowest}, \tag{15}$$

  where H_{ave} is the elevation of the centroid point, and the H_{lowest} is elevation of the lowest point.

2.2.4. Other features

- Area O_{ar}

  The number of points in a segment is defined as area feature O_{ar}, which reflects the area of the segment.

- Slope O_{sl}

  This feature O_{sl} is computed as the included angle between the normal of a segment and a vertical vector. O_{sl} is shown in Figure 5d.

Overall, the extracted four groups of features are list in Table 1.

Table 1. The extracted features.

Features	Sign
Projection-area-based features	PR_t, PR_h
Eigenvalue-based features	$\lambda_1, \lambda_2, \lambda_3, \lambda_l, \lambda_p, \lambda_s, \lambda_a, \lambda_o, \lambda_e, \lambda_c$
Elevation-based features	H_r, H_v, H_{diff}, H_n
Others	O_{ar}, O_{sl}

2.3. Random Forests Based Feature Selection and Classification

2.3.1. Random Forests

The RF classifier [50] is an ensemble of a set of decision trees. These trees in RF are created by drawing a subset of training data through a bagging approach. The bagging randomly selects about two thirds of the samples from a training data to train these trees. This means that the same sample can be selected several times, while others may not be selected at all [51]. Then, the remaining samples are used in an internal cross-validation technique for estimating performs of RF. In addition, the Weighted Random Forest [59] method is utilized for solving the imbalanced sample problem in RF.

Two parameters, i.e., the number N_{tree} of trees and the number N_{feas} of features, are required for using a RF classifier. Then, each tree in RF is independently produced without any pruning. The number N_{feas} of features is used for training each tree. Each node in a tree is split by selecting N_{feas} features from the d-dimensional input feature space at random. The splitting function usually uses Shannon entropy or Gini index as a measure of impurity. In prediction, each tree votes for a class membership for each test sample, the class with maximum votes will be considered as the final class.

2.3.2. Feature Selection

The objective of feature selection is to identify a small set of discriminative features that can still achieve a good predictive performance [19]. The RF provides a measure VI_i of variable importance based on averaging the permutation importance measure of all the trees which is shown to be a reliable indicator [60]. The permutation importance measure is based on Out-Of-Bag (OOB) errors, and is utilized to select features.

Herein, we use the variable importance measure in RF and the backward elimination method [52] to select features. The backward elimination method removes the most relevant features by iteratively fitting RF. In our approach, only one feature with the lowest importance value is eliminated at each iteration, and then a new forest is built by the remained N_{rmf} features. At the end of each iteration, we compute the mean decrease permutation accuracies [19] VI_i for $i = 1 \ldots N_{rmf}$ and rank the remained features by them. To measure the importance of the remained features at each iteration, the overall mean decrease permutation accuracy OD_k is computed by averaging all the remained features' importance values. OD_k is computed as follow:

$$OD_k = \frac{1}{N_{rf}} \sum_{i=1}^{N_{rmf}} VI_i \text{ for } k = 1 \ldots N_{bi} \tag{16}$$

where k corresponds to the iteration times, and N_{bi} is the total number of iterations. The iterative procedure stops and all the RFs are fitted when N_{rmf} is equal to N_{feas}.

After all the RFs are fitted, we computed the range I_r between the maximum and the minimum overall mean decrease permutation accuracies ($OD_{max} = \max(OD_k)\ for\ k = 1 \ldots N_{bi},\ and\ OD_{min} = \min(OD_k)\ for\ k = 1 \ldots N_{bi}$). Then, we select a critical point according to the variation tendency of OD_k. In this paper, the principle of the selection is that the variation of OD_k caused by the eliminated features should be lower than 20%, i.e., the critical point which divides the range I_r by a ratio of at least 8:2 is selected. At last, we select the most important features according to the critical point and the backward elimination results.

2.3.3. Supervised Classification

After the feature selection, the training samples with selected feature set are utilized to train a RF classifier, and the classifier is used to predict the labels of unlabeled segments.

2.4. Post-Processing

There may be some misjudgments in the above initial classification results. Actually, both natural and artificial objects generally have been associated with specific semantic information. For example, cars occupy small areas and are parked on ground, most of building roofs are composed of planar faces and have relatively large area, and wires are elevated over ground. Moreover, semantic information is more convenient to be detected via segments than individual points. Therefore, semantic information is utilized to define several rules for optimizing the initial results. Note that the post-processing stage cannot correct all the misjudgments.

To define the semantic rules, two types of neighborhoods are determined. The first one $Ngbr_1$ is determined in 3D space, and the second one $Ngbr_2$ is determined in XY-plane. In the post-processing stage, if we find a misjudged segment based on these rules, we first detect labels of its adjacent segments based on $Ngbr_1$, then we relabel it as the class which arises the most times. Herein, we only list the useful rules for our approach. The rules for each class are shown as follows.

(1) Rule for ground

- In the neighborhood $Ngbr_1$ of a query ground segment S_{gs}, S^i_{ga1} for $i = 1, 2, \ldots, N_s$ is the i-th adjacent segment. The elevation difference between each segment pair containing S_{gs} and S^i_{ga1} is in a small interval Int_{gs}.
- In the neighborhood $Ngbr_2$ of a query ground segment S_{gs}, there is no adjacent segment $S^i_{ga2}, i = 1, \ldots, N_s$ whose maximum elevation much lower than the minimum elevation of S_{gs}.
- Considering an extreme case, if we want to obtain a high precision DTM from a complex mountainous region, we can combine the initial ground segments with the segment-based PTD (progressive TIN densification) filtering method [61] or a progressive graph cut method [62]. First, the ground segments in the initial classification result are considered as latent ground segments. Next, a 2D grid is constructed with a bin size equal to the maximum building size. Then, a latent ground segment which contains the lowest point in each bin is recognized as a ground seed segment. Finally, points in the ground seed segments are utilized to construct a TIN as the initial ground surface, and ground points will be extracted by a PTD or a progressive graph cut method.

(2) Rule for building roofs

In the neighborhood $Ngbr_1$ of a query building roof segment S_{bs}, it has the same characteristics as ground. However, in the neighborhood $Ngbr_2$, we can find an adjacent segment $S^i_{ba2}, i = 1, \ldots, N_s$ whose maximum elevation is much lower than the minimum elevation of S_{bs}, the elevation difference threshold of this elevation difference is denoted as D_{mm}.

(3) Rule for vehicles

- A car segment should have a certain range of area: $[Ar_{vmin}, Ar_{vmax}]$.
- In the neighborhood $Ngbr_1$ of a query car segment S_{vs}, there is at least one adjacent segment $S^i_{va1}, i = 1, \ldots, N_s$ labeled as ground.

(4) Rule for wires

- In the neighborhood $Ngbr_1$ of a query wire segment S_{ps}, there is no adjacent segment $S_{pa1}^{i}, i = 1, \ldots, N_s$ with a label of ground or car.
- The 3D shape of a wire segment can be linear or planar, however, cannot be volumetric.

(5) Rule for vegetation

- Vegetation segments are often confused with vehicle segments. Besides, the misjudged segments in the initial classification result tend to arise in high vegetation rather than low vegetation. Therefore, the misjudged segments in high vegetation are able to be corrected by the rules for vehicles simultaneously.
- Considering an extreme case, we assume that some vehicle segments are misjudged as low vegetation segments. First, a misjudged query segment should have a neighbor labeled as ground, then, if the height, width and length of the segment are in certain ranges $\left[T_{Car_H^{min}}, T_{Car_H^{max}}\right]$, $\left[T_{Car_W^{min}}, T_{Car_W^{max}}\right]$, $\left[T_{Car_L^{min}}, T_{Car_L^{max}}\right]$, the segment will be relabeled as vehicle. The thresholds of these ranges are cited from the approach in literature [24]. Besides, the height, width and length of a segment are computed in a local coordinate framework composed of v_1, v_2 and v_3. The v_1, v_2 and v_3 are eigenvectors of the covariance matrix M constructed by points in the segment as formula (3).

3. Experiments and Discussions

We developed a protype framework for the proposed segment-based point cloud classification method using C++ language and Point Cloud Library (PCL) [63]. We also implemented segment-based point cloud classification using SVM and the RG segmentation [57], in which the open source libSVM [64] is used for the implementation of SVM and PCL is used for the implementation of RG segmentation.

The experiments are conducted on a workstation running Microsoft Windows 7 (×64) with two 16-Core Intel Xeon E5-2650, 64GB Random Access Memory (RAM) and 3TB hard disk.

There are two parts in the experiments and discussions. The first part is experimental setting which includes study areas and evaluation metrics. The second part is results and discussions which are presented in Sections 3.2–3.6.

In the second part, there are three improvements compared with existing classification methods, i.e., the step-wise point cloud segmentation, the integration of RF and the segment-based classification, and the employment of semantic rules in the post-processing stage. Therefore, we first discuss the impact of the three improvements and analyze the advantages of them in Sections 3.2–3.4. Then, the classification results and accuracies of the protype framework are shown in Sections 3.5 and 3.6. Note that the classification results should be presented after the discussion of the three improvements. Because the classification results are obtained by the parameters which are determined by the discussion in Sections 3.2–3.4.

3.1. Experimental Setting

3.1.1. Study Areas

Three study areas are involved in our experiments. The first one is selected from a publicly available ALS dataset which is obtained by the University of Iowa in 2008 [65]. The data are collected to survey the Iowa River Flood along the Iowa River and Clear Creek Watershed. The data collection is funded by NSF Small Grant for Exploratory Research (SGER) program. Area 1 is shown in Figure 6a and it contains 1,512,092 points with an average point spacing of 0.6 m. In Figure 6a, the point cloud of Area 1 is colored by elevation. In this area, the ground is flat and smooth. On the ground, there are some parking lots where many vehicles are parked. In addition, some vehicles are parked under tree crowns, or close to houses. Buildings in this area are composed of several planar faces with different geometric shapes and a number of building elements such as chimneys. Several wires are intersected, and cross the trees with high elevation. Most trees and building roofs are overlapped. After the step-wise point cloud segmentation performed, 5949 segments are extracted from Area 1. 250 segments are selected as training samples for the RF classifier. Details of the training samples in Area 1 are shown in Table 2. Specifically, only one sample is selected for the class *ground*. Ground in Area 1 is flat and smooth, and points on the ground are clustered into only one segment by the step-wise point cloud segmentation.

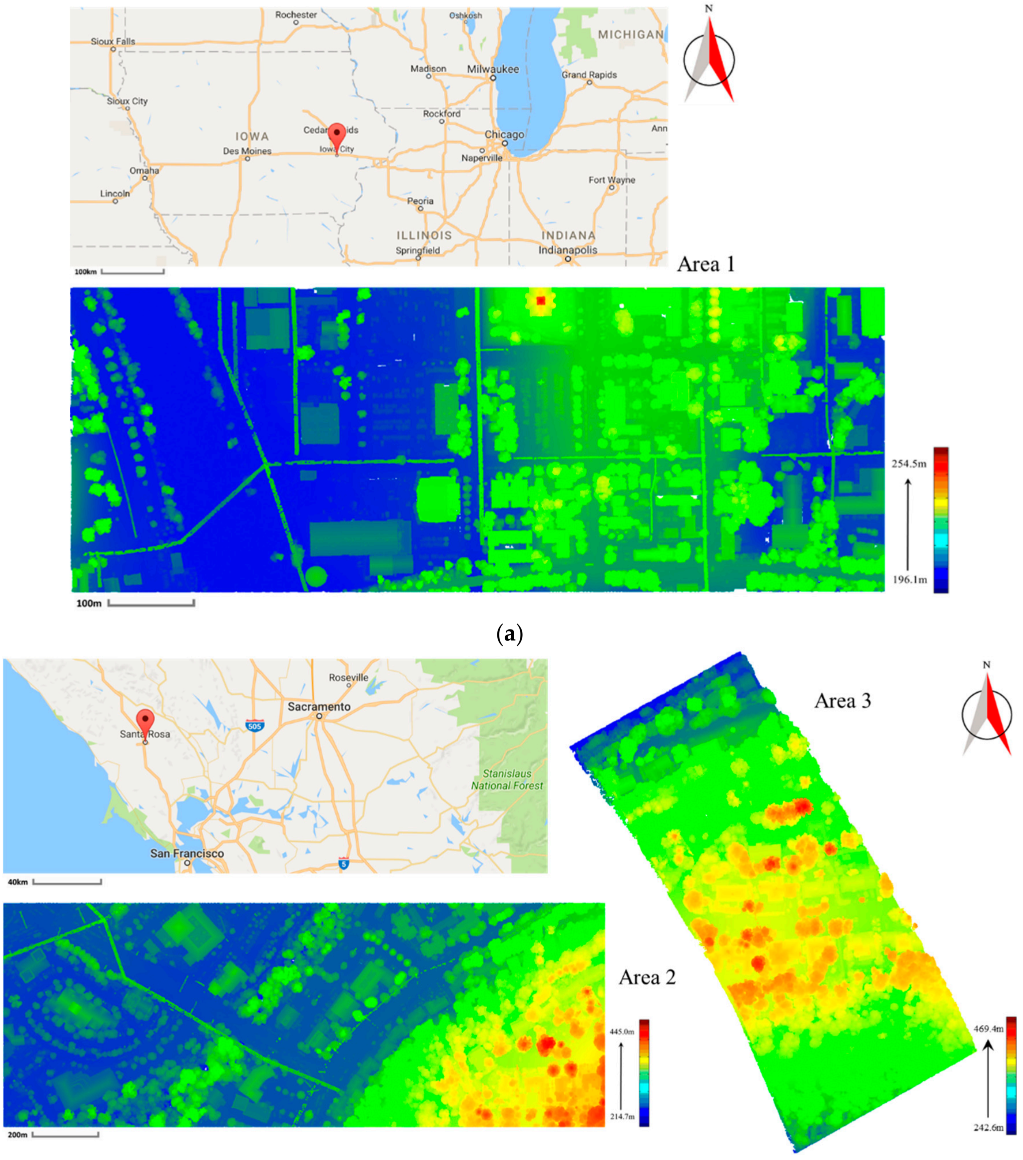

(**a**)

(**b**)

Figure 6. The testing data, (**a**) shows the point cloud of Area 1, (**b**) shows the point clouds for Area 2 and 3.

The second one is selected from a publicly available ALS dataset which is collected in Sonoma County [66] between 28 September and 23 November 2013 by the Watershed Sciences, Inc. (WSI). The dataset is provided by the University of Maryland and the Sonoma Country Vegetation Mapping and Lidar Program under grant NNX13AP69G from NASA's Carbon Monitoring System. Area 2 is shown in Figure 6b and it contains 1509228 points with an average point spacing of 1.0 m. In Figure 6b, the point cloud of Area 2 is colored by elevation. In this area, there is a mountain which is full of trees and ornamented by several houses. Buildings are overlapped with tree canopies significantly. Moreover, building elements such as skylights have complex 3D structure. Wires go across the trees have high elevations and are intersected with each other. A large number of vehicles are parked under tree crowns or near low vegetation. After the step-wise point cloud segmentation performed, 10697 segments are extracted from Area 2. 414 segments are selected as training samples for the RF classifier. Details of the training samples in Area 2 are shown in Table 2. Specifically, the number of training samples for the class *ground* is smaller than other classes. Although a mountain exists in Area 2, a majority of ground regions are flat and smooth. Therefore, points on ground in Area 2 are clustered into a smaller number of segments than other classes.

Table 2. Number of training samples (segments) per class for the three study areas.

Data	Class					
	Ground	Building	Vegetation	Vehicle	Wire	∑
Area 1	1	47	107	65	30	250
Area 2	4	66	228	94	22	414
Area 3	19	65	81	-	-	165

The third one is selected from the same dataset of Area 2. Area 3 is shown in Figure 6b and it contains 685870 points with an average point spacing of 1.0 m. In Figure 6b, the point cloud of Area 3 is colored by elevation. In this area, all the points are on a mountainous ground which is full of trees and ornamented by several houses. Area 3 is utilized to test the transplanting of the proposed classification framework to mountainous areas. There are only three types of objects, i.e., ground, buildings and vegetation. The ground of Area 3 is rugged with step edges. All the buildings are surrounded by vegetation. After the step-wise point cloud segmentation performed, 6658 segments are extracted from Area 3. 165 segments are selected as the training samples for the RF classifier. Details of the training samples in Area 3 are shown in Table 2. Specifically, the number of training samples for the class *ground* in Area 3 is larger than those in Area 1 and 2 because of the complex topographies.

In this paper, we classify Area 1 and 2 into five classes, i.e., *ground*, *building*, *vegetation*, *vehicle* and *wire*, and Area 3 into three classes, i.e., *ground, building and vegetation*. Area 1 and 2 are utilized to analyze the impact of the step-wise point cloud segmentation, the integration of RF and segment-based classification method, and the post-processing stage. Area 3 is employed to analyze to the classification result of a mountainous area with complex topographies.

To quantitatively analyze the classification accuracy, we obtain ground true for the three study areas by manual labelling. The details of the ground true for the three study areas are shown in Table 3. Note that quantitative analysis is derived by individual points rather than segments, because the hypothesis that no error exists in segments is unreasonable. Therefore, we present the ground true using individual points rather than segments.

Table 3. Number of points per class in ground true of the three study areas.

Data	Class					
	Ground	Building	Vegetation	Vehicle	Wire	∑
Area 1	949,431	218,835	309,889	24,138	9799	1,512,092
Area 2	589,231	227,442	651,022	36,520	5013	1,509,228
Area 3	202,755	64,337	418,778	-	-	685,870

3.1.2. Evaluation Metrics

For evaluation, we employ the confusion matrix and consider five commonly used measures: overall accuracy OA, Kappa coefficient $KA.$, precision P, recall R, and F_1-score. They are computed according to the confusion matrix as follows:

$$OA = \frac{\sum_{i=1}^{m} tp_i}{N}, \tag{17}$$

$$KA = \frac{N\sum_{i=1}^{m}(tp_i) - \sum_{i=1}^{m}((tp_i + fp_i) \times (tp_i + fn_i))}{N^2 - \sum_{i=1}^{m}((tp_i + fp_i) \times (tp_i + fn_i))} \tag{18}$$

$$P = \frac{tp_i}{tp_i + fp_i} \tag{19}$$

$$R = \frac{tp_i}{tp_i + fn_i} \tag{20}$$

$$F_1 = 2 \cdot \frac{P \cdot R}{P + R} \tag{21}$$

where tp_i is the main diagonal element in i-th row, fp_i is computed from the sum of i-th column, excluding the main diagonal element, fn_i is the sum along i-th row, excluding the main diagonal element, m is the number of classes, and N is the number of all the points in an input point cloud.

3.2. Impact of the Step-Wise Point Cloud Segmentation

Our proposed step-wise point cloud segmentation method can extract three kinds of segments, i.e., planar, smooth and rough surfaces. We compare our method with the RG method [57], which has been published in PCL. The PCL supplies two kinds of processes based on the RG method. The first one is designed for plane extraction (RG-based plane segmentation) and the second one is designed for smooth surface extraction (RG-based smoothness segmentation). Six parameters in RG method published in PCL are used, i.e., the number k_n of neighbors for normal estimation, the number k_g of neighbors for growing, the smoothness threshold th_θ, the curvature threshold th_c, the residual threshold th_r, and the minimum size threshold s_{min}.

3.2.1. Qualitative Comparison

To visually compare our segmentation method with the RG methods, we select a small part from Area 1 to present the segmentation results. The parameter setting of our segmentation method is shown in Table 4 and the parameter setting of the RG method is shown in Table 5. Figure 7 presents the comparison of these segmentation results. We can find that our segmentation method not only can detects three kinds of segments, but also can clusters the ground points into a small number of segments, especially a single segment. Besides, intersecting planes, building roofs covered by vegetation, and small or narrow planes can be extracted by our segmentation method (see Figure 7a). The plane segmentation has the following shortcomings: (1) The segmentation result of the intersection between two planes is insufficient; (2) Small objects such as cars cannot be extracted; (3) Most majority of scattered points such as tree points cannot be segmented. The smoothness segmentation has the following shortcomings: (1) Intersected planes cannot be divided; (2) Small objects such as cars cannot be extracted, although it is implemented to extract smooth surfaces; (3) The building points and tree points could be clustered into the same region if they overlap with each other.

Table 4. The parameter setting of our method for a small part in Area 1.

Parameters	k_n	d_r	th_θ	s_{min}	k_p	d_{max}	th_{sp}
Our method	50	0.1	0.1	30	15	1.0	1.5

Table 5. The parameter setting of RG method for a small part in Area 1.

Parameters	k_n	k_g	th_θ	th_c	th_r	s_{min}
RG-based plane segmentation	50	50	0.1	0.1	0.3	0
RG-based smoothness segmentation	50	50	0.1	0.1	0.5	0

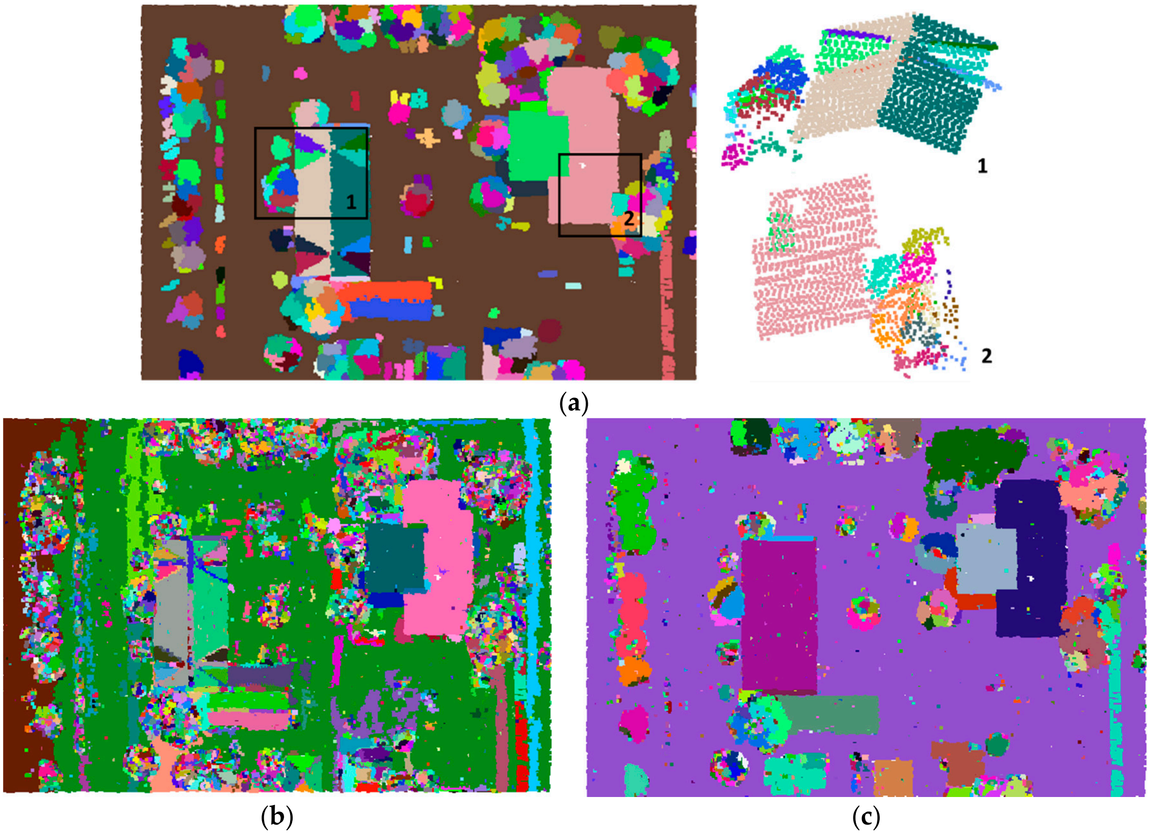

Figure 7. Comparison of our segmentation method with the RG methods presented in Point Cloud Library (PCL): (**a**) The result of our method; (**b**) The result of the RG-based plane segmentation; (**c**) The result of the RG-based smoothness segmentation.

3.2.2. Quantitative Comparison

To quantitatively analyze the advantages of our segmentation method, the entire data of Area 1 and Area 2 are utilized. The time costs of our proposed segmentation method for processing Area 1 and 2 are 3.7 min and 4.4 min, respectively. We compare our method with the RG methods in terms of the classification measure F_1 score. In order to facilitate an objective comparison, all results based on the RG methods are averaged over 20 runs. The parameter setting of the step-wise point cloud segmentation method is shown in Table 6. The F_1-score comparison is shown in Figure 8. The red bar describes the F_1-score of our segmentation method, while the green bar describes the F_1-score of the RG-based smoothness segmentation method, and the blue bar describes the F_1-score of the RG-based plane segmentation. All classes' F_1-score values of our segmentation method are larger than those of the RG methods for both Area 1 and 2. Specially, the F_1-score values of the class *vehicle* derived by our method are significantly higher. The reason is that our segmentation method clusters all the points in a small-scale object into a few segments.

Table 6. The parameter setting of our method for Area 1 and 2.

Parameters	k_n	d_r	th_θ	s_{min}	k_p	d_{max}	th_{sp}
Area 1	50	0.1	0.1	30	15	1.0	1.5
Area 2	50	0.1	0.1	30	15	3.0	2.0

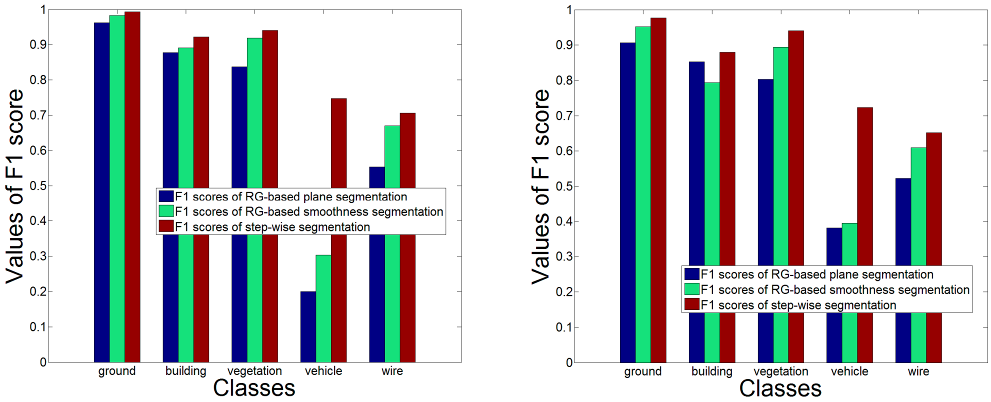

(**a**) (**b**)

Figure 8. All classes' F_1-score values of different segmentation methods for Area 1 and Area 2: (**a**) F_1-score values of Area 1; (**b**) F_1-score values of Area 2.

3.3. The Integration of RF and Segment-Based Classification

3.3.1. Parameter Tuning for Random Forests

The two parameters in the RF classifier, i.e., N_{tree} and N_{feas} are utilized not only in the classification procedure, but also in the feature selection task. In the feature selection task, N_{feas} is set to 4 according to the existing studies [19,38], which is a default setting and turned out to be a good choice of OOB rate [19]. However, different studies have different settings of N_{tree}. Therefore, we have to unfold a test before feature selection for finding an appropriate value of N_{tree}. Besides, this test is also meaningful for supervised classification tasks in which the setting of N_{tree} is still stochastic [23].

To find an appropriate value of N_{tree} for a stable classification, we test the classification procedure with N_{tree} varying from 100 to 1000 and N_{feas} from 1 to 9. For evaluating the classification results, we utilize overall accuracy and Kappa coefficient to analyze the overall performance. Figure 9a,b show the variation tendency of overall accuracy and Figure 9c,d show the variation tendency of the Kappa coefficient. To make them more concise, we compute the mean and the standard deviation of the derived overall accuracy and kappa coefficient values under different settings of N_{tree} (see Figure 10a–d). The stability of the classification result will increase with an increasing value of N_{tree}. It is surprising that the overall accuracy and Kappa coefficient increase rapidly and the standard deviation decreases markedly with the augment of N_{tree} until it reaches 400. This case occurs in both Area 1 and Area 2. It may be the reason that 500 is the default value of N_{tree} in the R package for random forests [51]. Therefore, setting N_{tree} to 400 is reasonable in our approach, especially for decreasing the computational burden.

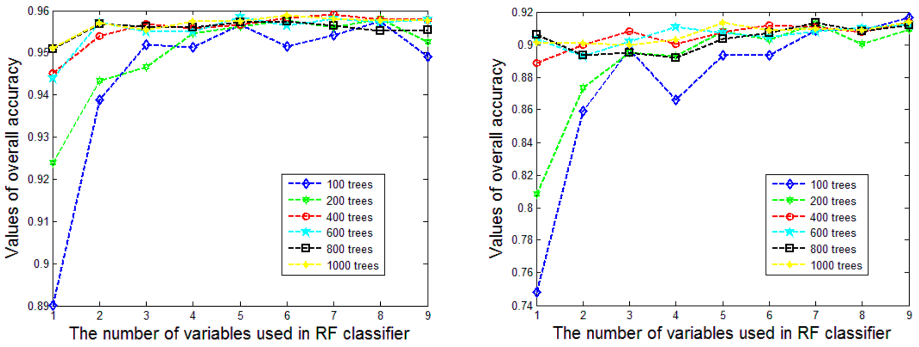

(**a**) (**b**)

Figure 9. *Cont.*

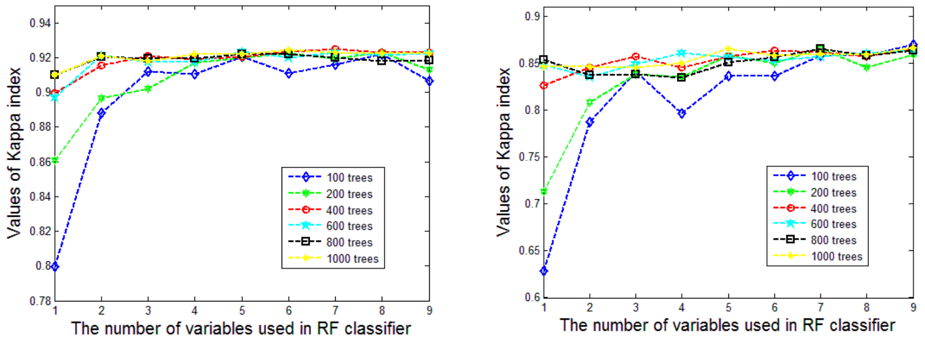

(**c**) (**d**)

Figure 9. The variation tendencies of overall accuracy and Kappa coefficient under different settings of N_{tree}: (**a**,**b**) are for Area 1 and Area 2 respectively; (**c**,**d**) are for Area 1 and Area 2 respectively.

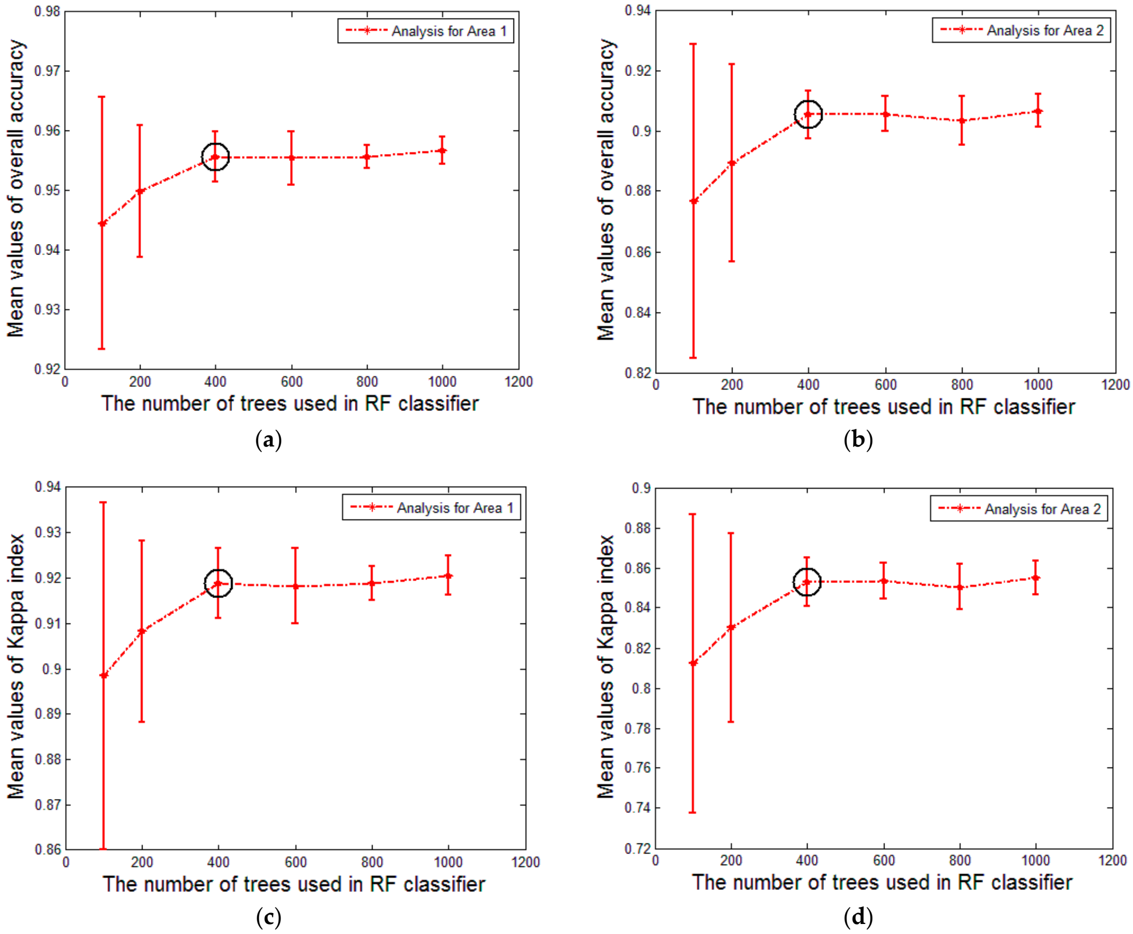

(**a**) (**b**)

(**c**) (**d**)

Figure 10. The variation tendencies of mean overall accuracy values and standard deviation values of overall accuracy and Kappa coefficient under different settings of N_{tree}; (**a**,**b**) are for Area 1 and Area 2 respectively; (**c**,**d**) are for Area 1 and Area 2 respectively.

3.3.2. RF-Based Feature Selection

To select features, we utilize the backward elimination method and iteratively fit a RF with the aforementioned parameter setting. In each fitted RF, the importance of each feature is estimated. Figure 11 shows all the feature importance values of Area 1 and 2 which are estimated in the first time fitting.

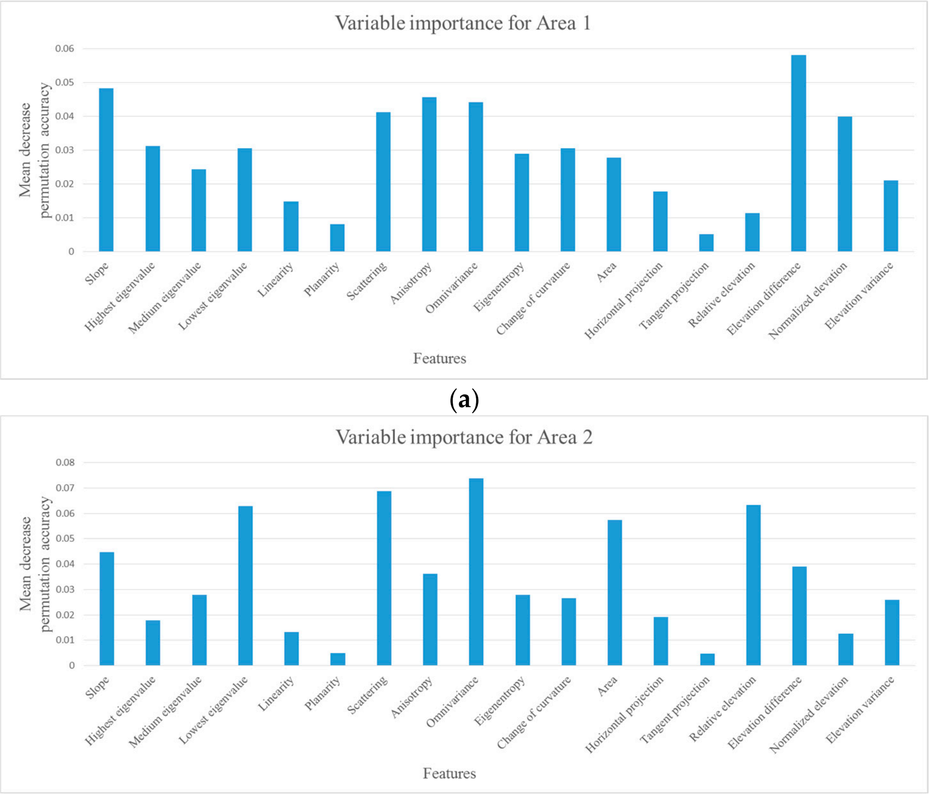

(**a**)

(**b**)

Figure 11. Feature importance values based on the mean decrease permutation accuracy estimated by the first time fitted RF: (**a**) is for Area 1; (**b**) is for Area 2.

The backward elimination method first fits a RF from the feature set S_{feas}, then the feature with the lowest importance value is eliminated from S_{feas}. The two steps are iterated until the number of features in S_{feas} is equal to 4. Subsequently, we select features based on the eliminating order.

To determine the number of independent features, we present the variation tendency of the overall mean decrease permutation accuracy OD_k in Figure 12. For Area 1 (see Figure 12a), the maximum overall mean decrease permutation accuracy OD_{max} is 0.1834, and the minimum overall mean decrease permutation accuracy OD_{min} is 0.03426. When only 11 features are remained, the overall mean decrease permutation accuracy OD_i is 0.05864, which divides the range I_r with a ratio no less than 8:2. Besides, the tendency in Figure 12a decreases rapidly until the remained feature number reaches 11. For Area 2 (see Figure 12b), the maximum overall mean decrease permutation accuracy OD_{max} is 0.2215, and the minimum overall mean decrease permutation accuracy OD_{min} is 0.03991. When only 10 features are remained, the overall mean decrease permutation accuracy OD_i is 0.07588, which divides the range I_r with a ratio no less than 8:2. However, the tendency of Figure 12b decreases rapidly from 10 to 11 remained features, therefore, we select 11 features for Area 2 as a compromised solution. According to the aforementioned analysis, the number 11 of independent features is reasonable for both Area 1 and 2.

According to the aforementioned procedure, the selected features for Area 1 are slope O_{sl}, lowest eigenvalue λ_3, elevation difference H_{diff}, scattering λ_s, change of curvature λ_c, eigenentropy λ_e, omnivariance λ_o, anisotropy λ_a, highest eigenvalue λ_1, normalized elevation H_n and area O_{ar}.

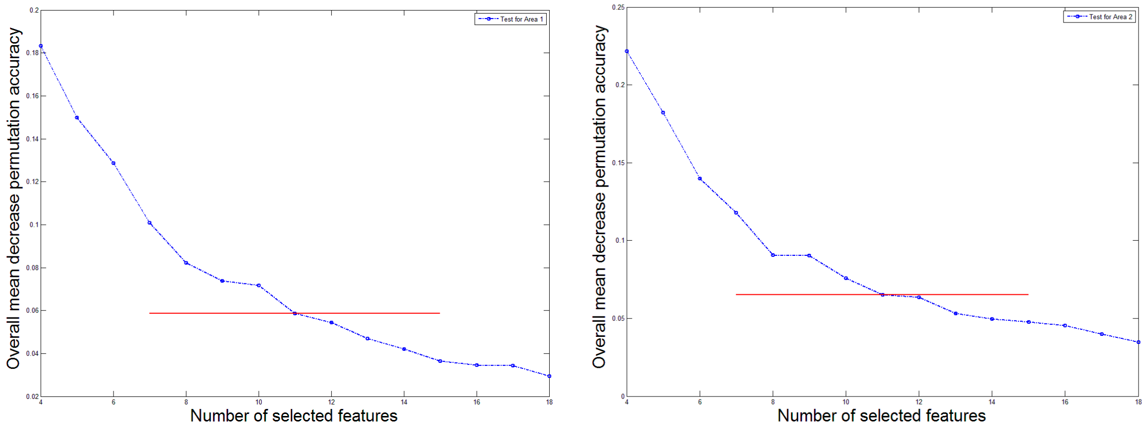

(**a**) (**b**)

Figure 12. Feature selection via iterative elimination for Area 1 and 2 based on the overall mean decrease permutation accuracy: (**a**) is for Area 1; (**b**) is for Area 2.

The selected features for Area 2 are scattering λ_s, area O_{ar}, elevation difference H_{diff}, lowest eigenvalue λ_3, omnivariance λ_o, relative elevation H_r, slope O_{sl}, anisotropy λ_a, medium eigenvalue λ_2, eigenentropy λ_e and normalized elevation H_n. The selected features are listed in elimination orders for Area 1 and 2 respectively.

3.3.3. Robustness of the Integration of RF and the Segment-Based Classification

To test this robustness and the stability of the integration of RF and the segment-based classification, we add some noisy vectors to the computed feature set. It is worth noting that we do not record which feature vector is noisy, and therefore, we do not know which one is the noisy vector in the feature set when we train a RF and make prediction. Then, we analyze the overall accuracy and Kappa coefficient values of the classification results with different numbers of noisy vectors.

Besides, we implement the integration of SVM and the segment-based classification presented in [36] and analyze its robustness. It is worth noting that both the two integration methods have no complemental step for dealing with noises. To impartially compare the robustness of the two integrations, the feature selection procedure in our method is not performed, due to the fact that feature selection is not employed to the integration in [36].

As shown in Figure 13, when there is no noisy feature vector, the two integration methods get the classification results with similar overall accuracy and kappa coefficient values. When the noisy vector number is increasing, the values of the integration presented in the literature [36] decrease. Besides, our method obtains a mean standard deviation 0.0014 of overall accuracy values (0.0017 for Area 1 and 0.0012 for Area 2), and a mean standard deviation 0.0024 of kappa coefficient values (0.003 for Area 1 and 0.002 for Area 2), with the noisy feature vector number from 0 to 10.

In a close-up theoretical inspection, when RF classifier splits a subset of features in a node, it finds a feature with the maximum entropy or Gini decrease. In this case, the noisy features can be eliminated and the best feature corresponding to the maximum decrease is selected. Therefore, our method which integrates RF with the segment-based classification is more stable and robust.

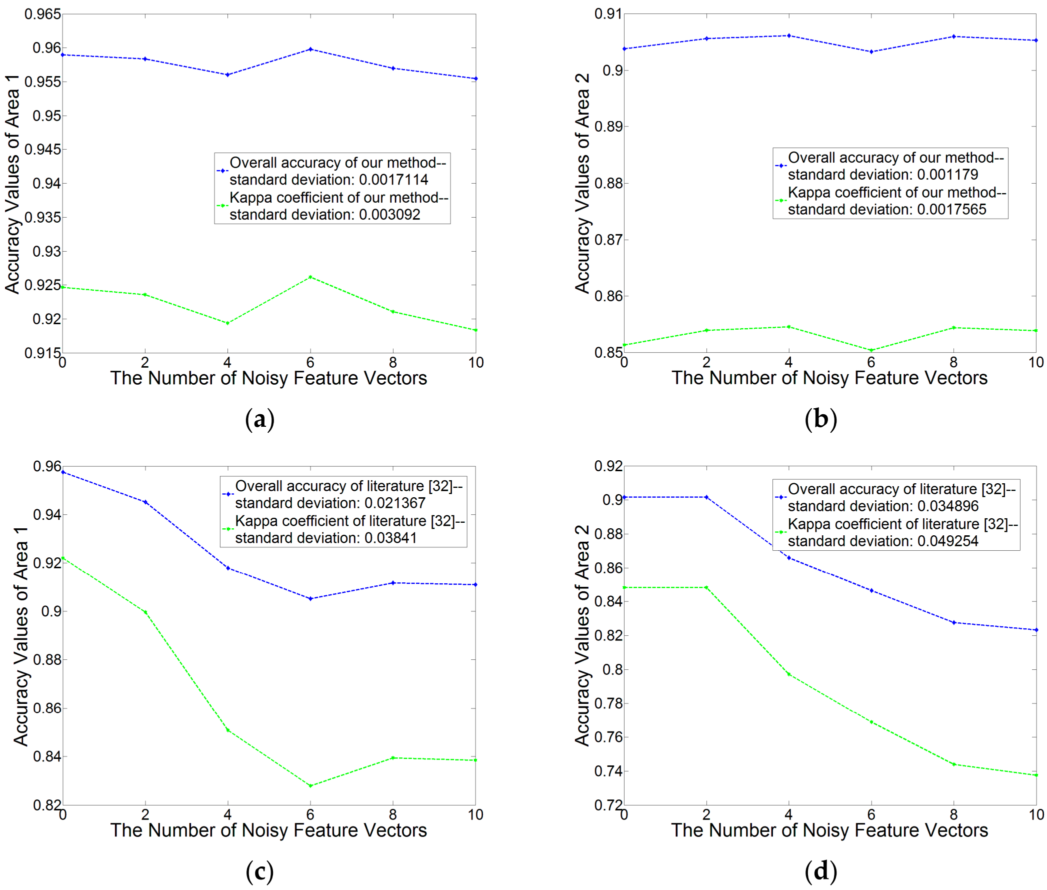

Figure 13. Comparison between the two integrations under different numbers of noisy feature vectors, (**a**,**b**) depict the accuracy values of our method for Area 1 and 2 respectively, (**c**,**d**) depict the accuracy values of the literature [36] for Area 1 and 2 respectively.

3.4. Impact of the Post-Processing Stage Based on the Semantic Rules

After the supervised classification, an initial classification result is obtained, in which misjudged segments may exist. In the post-processing stage, we first define several semantic rules for each class, and then utilize them to optimize the initial classification result. Note that the utilized semantic rules may be different for different input data, and the post-processing stage cannot correct all the misjudgments, however is an optimizing procedure. The rules for ground and the rule 2 for vegetation are not employed when we optimize Area 1 while others are employed. The rule 3 for ground and the rule 2 for vegetation are not employed when we optimize Area 2 while others are employed. Some thresholds are utilized to constrain the optimization which are list in Table 7. These threshold values are determined based on the natural form of an object and the point spacing of the input point cloud.

Table 7. The threshold values for the post-processing stage used for Area 1 and 2.

	Int_{gs}	Ar_{cmin}	Ar_{cmax}	D_{mm}
Area 1	—	10	500	2.5
Area 2	2.0	10	300	3.0

To qualitatively analyze the impact of the post-processing stage, we select two small areas in Area 1 and 2 respectively. Figure 14 shows the initial and the final results of the small areas. In the initial classification results (see Figure 14a,c), a number of segments are mislabeled as the class *vehicle* or *wire*. For example, building elements such as chimneys are often mislabeled as *vehicle*, tree segments with small size are often mislabeled as the class *vehicle* or *wire*. In the post-processing stage, the second rule for vehicles can deal with the initial false results where other classes of objects are mislabeled as *vehicle*, the rules for wires can deal with the initial false results where tree segments are mislabeled as *wire*. In the final results presented in Figure 14b,d, the initial false results are corrected based on these semantic rules.

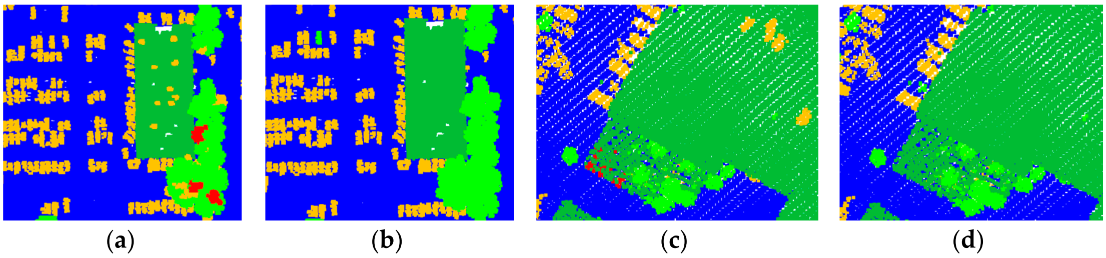

Figure 14. Analysis of the impact of the post-processing stage based on semantic rules: (**a**) The initial result of the first small area; (**b**) The final result of the first small area: (**c**) The initial result of the second small area; (**d**) The final result of the second small area.

For quantitative analysis, we compare each class's F_1-score for the initial results and the final results. Figure 15a,b show the F_1-score comparison for Area 1 and Area 2. We can find that the F_1-score of the class *vehicle* is improved obviously both in Area 1 and 2. Besides, the F_1-score values of other classes are also improved at different levels.

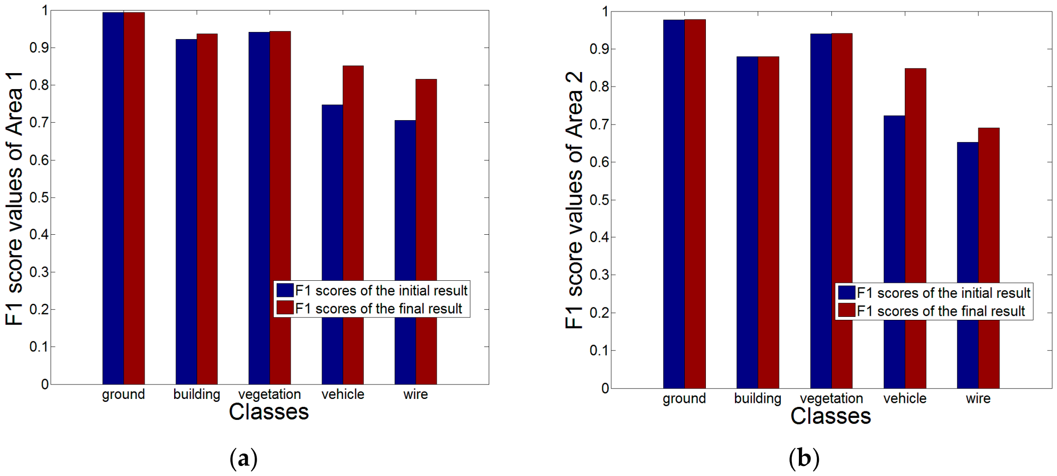

Figure 15. F_1-score comparison between the initial and final results of Area 1 and 2: (**a**) The comparison of Area 1; (**b**) The comparison of Area 2.

3.5. Classification Results and Accuracies

The final results of Area 1 and 2 are shown in Figure 16. The time costs of our proposed classification framework for processing Area 1 and 2 are 21 min and 25 min, respectively. The feature extraction procedure is the most time consuming step which costs 9 min and 12 min for Area 1 and 2, respectively. To quantitatively analyze the accuracies of classification, we compute the confusion matrix and the aforementioned five measures in Tables 8 and 9 based on the reference data generated by manual labelling. In addition, there may be missing points after the step-wise point cloud segmentation performed. These missing points will exist in the finial classification results and but are not labeled. In the quantitative evaluation, if some missing points belong to a class according to the ground true, they will be considered for evaluation. The revealed missing points are shown in the confusion matrices. Note that quantitative analysis is derived by individual points rather than segments, because the hypothesis that no error exists in segments is unreasonable.

As shown in Tables 8 and 9, the proposed method achieves a mean overall accuracy of 0.95255 (0.9697 and 0.9374 for Area 1 and 2 respectively), and a mean kappa coefficient of 0.9231 (0.9442 and 0.9020 for Area 1 and 2 respectively). The accuracy values of classes *ground*, *building* and *vegetation* are rather good. The accuracy values of *vehicle* and *wire*, are relatively lower than those of the other classes. The class *vehicle* achieves a mean F_1-score of 0.8504 (0.8519 and 0.8488 for Area 1 and 2, respectively), and the class *wire* achieves a mean F_1-score of 0.7531 (0.8155 and 0.6907 for Area 1 and 2, respectively).

The classification of small objects such as vehicles is the most challenging task. Generally, vegetation points make a 3D urban scene more complex and affect the classification of small objects. For example, wires often go across the trees with high elevation and vehicles are often parked near low vegetation or under tree canopies. Therefore, in the confusion matrices, vegetation points are often confused with another class points, and thus decrease the classification accuracy of other classes, especially for the classes of *vehicle* and *wire*. However, the accuracy of class *vegetation* achieves a mean F_1-score of 0.9422 (0.9429 and 0.9415 for Area 1 and 2, respectively) which is superior.

Table 8. The accuracy analysis of Area 1.

Overall Accuracy: 0.9697, Kappa Coefficient: 0.9442							
	Ground	**Building**	**Vegetation**	**Vehicle**	**Wire**	**Missing Points**	**Recall**
Ground	942,652	129	5546	463	32	609	0.9929
Building	2161	199,672	13,493	435	782	2292	0.9124
Vegetation	933	6514	296,124	1575	1038	3705	0.9556
Vehicle	1604	569	2053	19,771	67	74	0.8191
Wire	0	547	995	35	8067	155	0.8232
Precision	0.9950	0.9626	0.9306	0.8874	0.8078		
F_1-score	0.9939	0.9368	0.9429	0.8519	0.8155		

Table 9. The accuracy analysis of Area 2.

Overall Accuracy: 0.9374, Kappa Coefficient: 0.9020							
	Ground	**Building**	**Vegetation**	**Vehicle**	**Wire**	**Missing Points**	**Recall**
Ground	576,460	232	9337	201	225	2776	0.9783
Building	2837	187,101	28,992	282	306	7924	0.8226
Vegetation	8495	9737	616,655	4636	1042	10,457	0.9472
Vehicle	1467	629	3023	30,855	314	232	0.8449
Wire	0	37	846	206	3640	284	0.7261
Precision	0.9783	0.9462	0.9360	0.8528	0.6586		
F_1-score	0.9783	0.8801	0.9415	0.8488	0.6907		

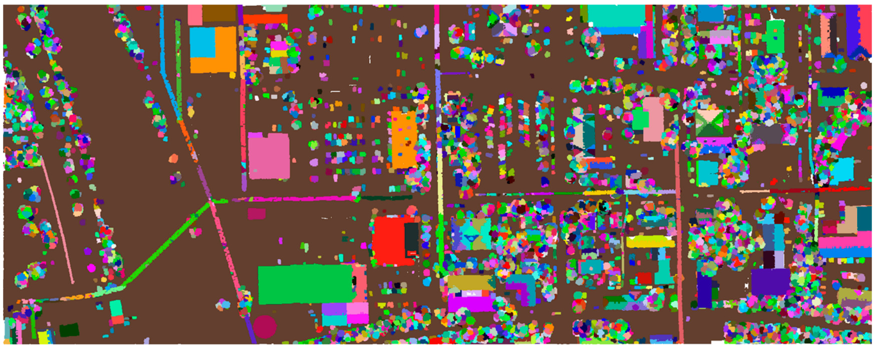

(**a**)

Figure 16. *Cont.*

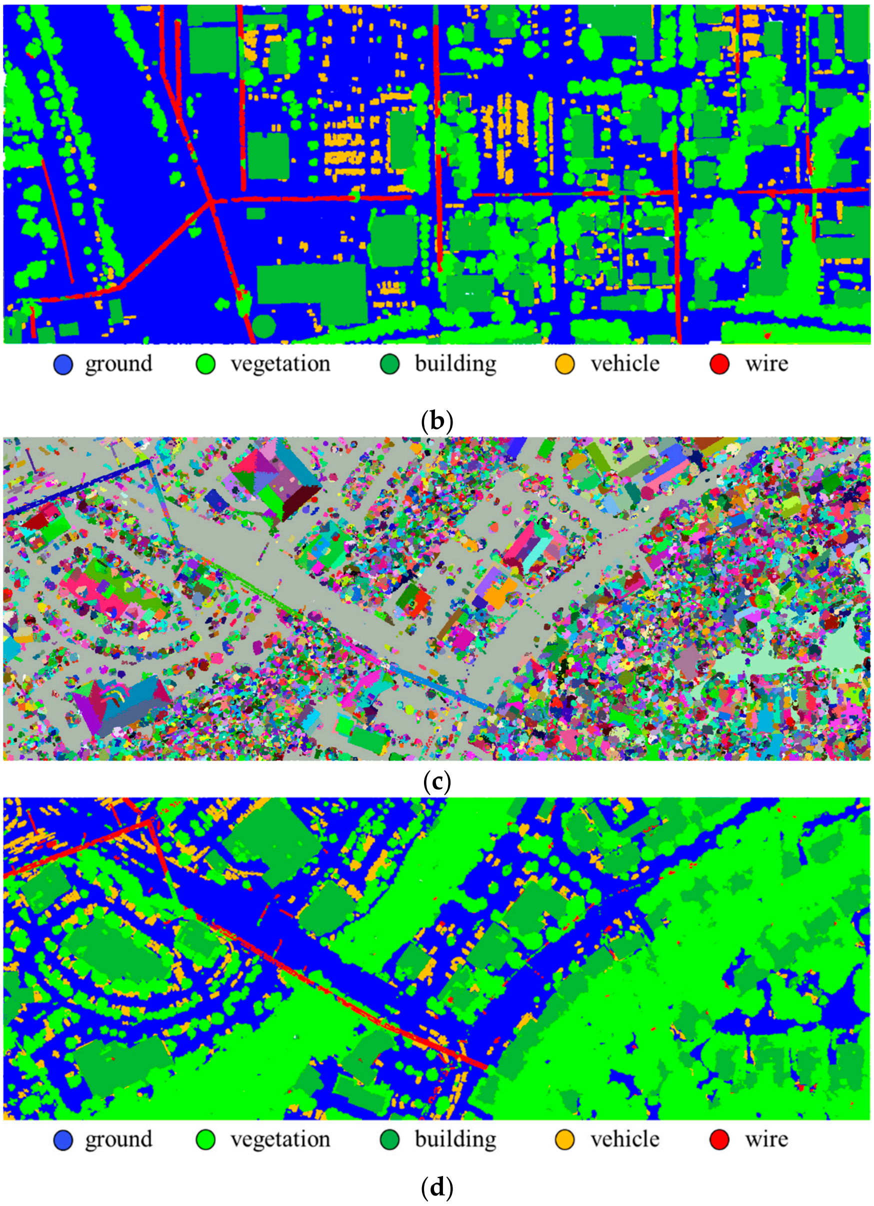

(**b**)

(**c**)

(**d**)

Figure 16. The results of the proposed classification framework for areas Area 1 and 2, (**a**) is the segmentation result of Area 1; (**b**) is the classification result of Area 1; (**c**) is the segmentation result of Area 2; (**d**) is the classification result of Area 2.

3.6. Transplantation to Mountainous Areas

To test the transplanting of the proposed method, extracted features and obtained parameters to mountainous areas, we classify a different 3D scene represented by Area 3. Area 3 is a mountainous area with step edges and rock faces. First, Area 3 is segmented by the proposed step-wise point cloud segmentation method with the same parameters as Area 2, and segment features are extracted. Next, a small feature set is selected by the obtained parameters of RF, i.e., $N_{tree} = 400$, and $N_{feas} = 4$. 9 features are selected by the backward elimination method presented in Section 3.3.2, and they are lowest eigenvalue λ_3, scattering λ_s, omnivariance λ_o, slope O_{sl}, change of curvature λ_c, planarity λ_p, anisotropy λ_a, eigenentropy λ_e, tangent plane projection area PA_t. Then, the ALS point cloud of Area 3 is classified by the select feature set. None of the semantic rules are utilized in the post-processing stage. 16 min are costed during the whole procedures among which the feature extraction procedure is the most time consuming step. The confusion matrix contained recall, precision, and F_1-score values is shown in Table 10, and its corresponding segmentation and classification results are shown in Figure 17.

Table 10. The accuracy analysis of Area 3.

Overall Accuracy: 0.9117, Kappa Coefficient: 0.8379					
	Ground	**Building**	**Vegetation**	**Missing Points**	**Recall**
Ground	182,090	4144	16,159	362	0.8981
Building	495	60,045	3485	312	0.9333
Vegetation	18,120	8568	383,143	8947	0.9149
Precision	0.9072	0.8253	0.9512		
F_1-score	0.9026	0.8760	0.9327		

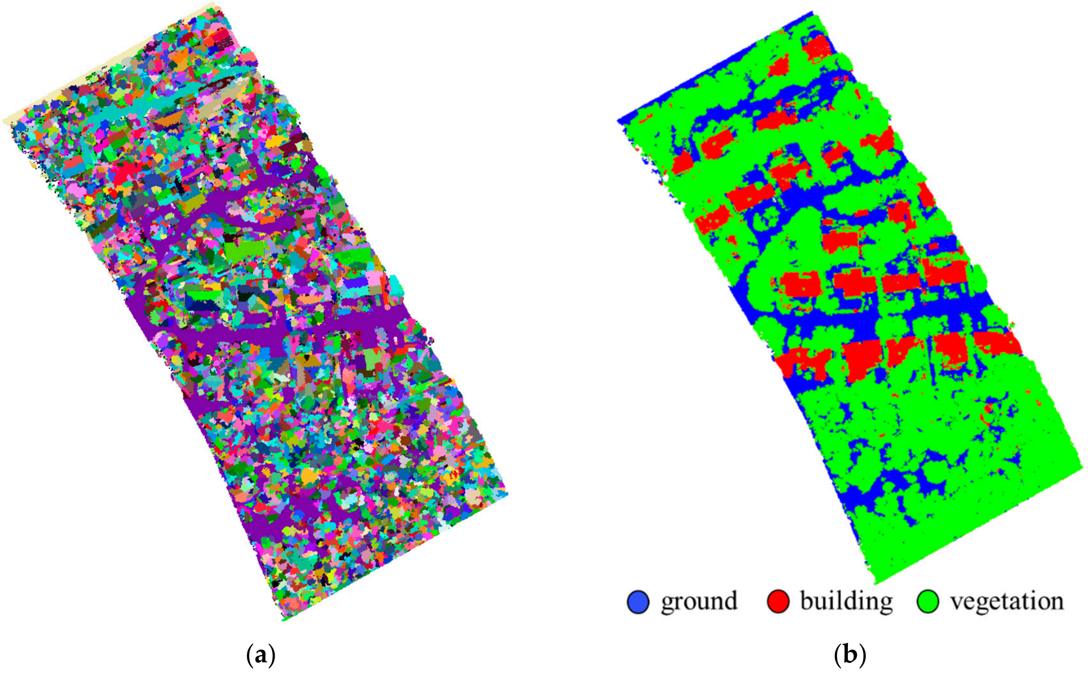

Figure 17. The results of the proposed classification framework for Area 3, (**a**) is the segmentation result of Area 3; (**b**) is the classification result of Area 3.

As shown in Table 10, the proposed classification framework and obtained parameters of RF achieve an overall accuracy of 0.9117, and a Kappa coefficient of 0.8379. The class *ground* achieves a F_1-score of 0.9026 which is lower than Area 1 and 2, because the ground of Area 3 is mountainous and rugged with step edges. The class *building* achieves a F_1-score of 0.8760, and the class *vegetation* achieves a F_1-score of 0.9327.

4. Uncertainties, Errors and Accuracies

The above experiments suggest that our proposed method obtains good results. There are three improvements in our proposed classification framework, which improve the accuracies of the classification results. However, there are still some errors in the classification results. We will list them according to missing points and the five aforementioned classes.

In the confusion matrices, the missing points appear more likely in the classes *building* and *vegetation*. For the class *vegetation*, the laser beam may penetrate the tree surface and collects a point in an internal branch. The internal point may be an isolated point, however, belong to the class *vegetation*. For the class *building*, the missing points often appear on building facades duo to the fact that building facades are incomplete and points in them are sparse in large-scale ALS point clouds.

For the class *ground*, uncertainties and errors are more likely to arise in the areas with mountainous and rugged topography. In Table 8, the class *ground* achieves a F_1-score of 0.9939 due to the fact that the ground in Area 1 is flat and smooth. In Table 9, the F_1-score of ground (0.9783) is lower than that of Area 1, because there is a hill that causes the topographical complexity increasing. In Area 3, all the ground points are located at a mountainous region which are rugged and full of step edges and rock faces. The F_1-score of class *ground* in Area 3 is 0.9026 which is much lower than those in Area 1 and 2. However, according to the recall and precision values of ground in Area 3, our proposed classification framework achieves the average accuracy of existing ALS point cloud filtering methods.

For the class *building*, the F_1-score (0.9368) in Area 1 is superior to those in Area 2 and 3. A close-up visual inspection shows that there are more buildings with vegetation confused in Area 2 and 3. Especially in Area 3, all the buildings are surrounded by vegetation and most of them are overlapped by tall trees. Although the regions where buildings and vegetation are confused are segmented correctly by the step-wise point cloud segmentation method, these regions still decrease the classification accuracy of the class *building*.

For the class *vegetation* in confusion matrix, vegetation points are often confused with other classes points. A close-up visual inspection shows that man-made objects such as buildings, vehicles and wires are often near vegetation. For example, buildings tend to be surrounded by trees, wires often go across tall trees. Therefore, vegetation makes a 3D scene more complex and affects the classification accuracy of other classes. However, the class *vegetation* achieves a mean F_1-score of 0.9390 (0.9429, 0.9415 and 0.9327 for Area 1, 2 and 3, respectively) which is superior due to the large cardinal number.

For the class *vehicle*, the mean F_1-score is 0.8504 (0.8519 and 0.8488 for Area 1 and 2, respectively) which is lower than the classes *ground*, *building*, and *vegetation*. Most misjudgments are caused by vegetation according to the confusion matrices, though the scene where vehicles are parked close to low vegetation is able to be correctly segmented. A close-up visual inspection shows that the mislabeled points always distribute randomly and irregularly. In an extreme case, it is inevitable that misjudgments exist in low vegetation which is in the same geometric form as a vehicle. However, the classification accuracy of the class *vehicle* is superior to the existing studies according to the analysis presented in Section 3.2.

For the class *wire*, the mean F_1-score is 0.7531 (0.8155 and 0.6907 for Area 1 and 2, respectively). The *wire* is the class with the lowest accuracy in our experiments. The wires in our study areas are rather common low voltage electrical wires than some special parts of overhead electric power transmission corridors. The misjudgments arise in the areas where wires go across trees. In these areas, wires and trees have similar point densities and cannot be divided by the segmentation method. Therefore, there will be a number of mislabeled points in the classification results of these areas, which affect the accuracy of the class *wire* most.

5. Conclusions

In this paper, we classify ALS point clouds via a framework with four stages, i.e., (i) step-wise point cloud segmentation; (ii) feature extraction; (iii) RF-based feature selection and classification; (iv) post-processing. In the first stage, the step-wise point cloud segmentation extracts three kinds of segments, i.e., planar, smooth and rough surfaces. Planar and smooth surfaces are more easy to characterize piecewise planar objects, and rough surfaces are more easy to characterize objects with irregular shapes. In the second stage, we extract geometric features from the input ALS point cloud by considering segments as the basic computational units. In the third stage, we integrate RF with the segment-based classification method to classify ALS point clouds. Discriminative features are selected using the backward elimination method based on OOB errors, and an appropriate value (400) for the number of trees used in RF is determined. At last, we employ semantic information to define several rules for each class, and utilize them in the post-processing stage to optimize the classification results.

There are two contributions in the framework, i.e., step-wise point cloud segmentation, and the integration of RF and the segment-based classification method. In the step-wise point cloud segmentation, we utilize a RANSAC method to optimize the normal vector and neighborhood of each point, and next grow a region among the optimized neighborhood for each seed point. Then, scattered points are detected and initial patches are constructed. Finally, the log Euclidean Riemannian metric is utilized as a constraint to connect the initial patches to rough surfaces. Experiments validate that the step-wise segmentation is good at recognizing small-scale objects. To analyze the integration of RF and the segment-based classification, we first find a suitable parameter setting of RF, then select features based on these parameters, and finally analyze the robustness and show the benefits of the integration.

There is a limit existing in our method, i.e., objects with less geometric distinguishability cannot be recognized, such as flat roads which has similar geometric attributes with ground. In future work, we will take more features and complemental strategies into consideration to classify these kinds of objects.

Acknowledgments: This research was funded by: (1) the General Program sponsored by the National Natural Science Foundations of China (NSFC) under Grant 41371405; (2) the Foundation for Remote Sensing Young Talents by the National Remote Sensing Center of China; (3) the Basic Research Fund of the Chinese Academy of Surveying and Mapping under Grant 777161103; and (4) the General Program sponsored by the National Natural Science Foundations of China (NSFC) under Grant 41671440.

Author Contributions: All of the authors contributed extensively to the work presented in this paper. Huan Ni proposed the step-wise segmentation methods and the classification framework, implemented all the algorithms presented in this manuscript, and wrote this paper. Xiangguo Lin discussed the structure of this manuscript, revised this manuscript, named this method, supported this research, and supplied experimental facilities. Jixian Zhang revised this manuscript, supported this research, and guided the overall studies.

Conflicts of Interest: The authors declare no conflict of interest.

References

1. Yan, W.Y.; Shaker, A.; El-Ashmawy, N. Urban land cover classification using airborne lidar data: A review. *Remote Sens. Environ.* **2015**, *158*, 295–310. [CrossRef]
2. Zhang, J.; Lin, X. Advances in fusion of optical imagery and lidar point cloud applied to photogrammetry and remote sensing. *Int. J. Image Data Fusion* **2017**, *8*, 1–31. [CrossRef]
3. Sithole, G.; Vosselman, G. Experimental comparison of filter algorithms for bare-earth extraction from airborne laser scanning point clouds. *ISPRS-J. Photogramm. Remote Sens.* **2004**, *59*, 85–101. [CrossRef]
4. Meng, X.L.; Currit, N.; Zhao, K.G. Ground filtering algorithms for airborne lidar data: A review of critical issues. *Remote Sens.* **2010**, *2*, 833–860. [CrossRef]
5. Chen, C.F.; Li, Y.Y.; Yan, C.Q.; Dai, H.L.; Liu, G.L.; Guo, J.Y. An improved multi-resolution hierarchical classification method based on robust segmentation for filtering als point clouds. *Int. J. Remote Sens.* **2016**, *37*, 950–968. [CrossRef]
6. Zhang, J.X.; Lin, X.G. Filtering airborne lidar data by embedding smoothness-constrained segmentation in progressive tin densification. *ISPRS-J. Photogramm. Remote Sens.* **2013**, *81*, 44–59. [CrossRef]
7. Yang, B.; Huang, R.; Dong, Z.; Zang, Y.; Li, J. Two-step adaptive extraction method for ground points and breaklines from lidar point clouds. *ISPRS-J. Photogramm. Remote Sens.* **2016**, *119*, 373–389. [CrossRef]
8. Lee, J.H.; Biging, G.S.; Radke, J.D.; Fisher, J.B. An improved topographic mapping technique from airborne lidar: Application in a forested hillside. *Int. J. Remote Sens.* **2013**, *34*, 7293–7311. [CrossRef]
9. Sampath, A.; Shan, J. Building boundary tracing and regularization from airborne lidar point clouds. *Photogramm. Eng. Remote Sens.* **2007**, *73*, 805–812. [CrossRef]
10. Chen, D.; Zhang, L.Q.; Mathiopoulos, P.T.; Huang, X.F. A methodology for automated segmentation and reconstruction of urban 3-d buildings from als point clouds. *IEEE J. Sel. Top. Appl. Earth Obs. Remote Sens.* **2014**, *7*, 4199–4217. [CrossRef]
11. Jarzgbek-Rychard, M.; Borkowski, A. 3d building reconstruction from als data using unambiguous decomposition into elementary structures. *ISPRS-J. Photogramm. Remote Sens.* **2016**, *118*, 1–12. [CrossRef]
12. Sampath, A.; Shan, J. Segmentation and reconstruction of polyhedral building roofs from aerial lidar point clouds. *IEEE Trans. Geosci. Remote Sens.* **2010**, *48*, 1554–1567. [CrossRef]

13. Yu, S.; Yu, B.; Song, W.; Wu, B.; Zhou, J.; Huang, Y.; Wu, J.; Zhao, F.; Mao, W. View-based greenery: A three-dimensional assessment of city buildings' green visibility using floor green view index. *Landsc. Urban Plan.* **2016**, *152*, 13–26. [CrossRef]
14. Polewski, P.; Yao, W.; Heurich, M.; Krzystek, P.; Stilla, U. Detection of fallen trees in als point clouds using a normalized cut approach trained by simulation. *ISPRS-J. Photogramm. Remote Sens.* **2015**, *105*, 252–271. [CrossRef]
15. Rodriguez-Cuenca, B.; Garcia-Cortes, S.; Ordonez, C.; Alonso, M.C. Automatic detection and classification of pole-like objects in urban point cloud data using an anomaly detection algorithm. *Remote Sens.* **2015**, *7*, 12680–12703. [CrossRef]
16. Wu, B.; Yu, B.; Wu, Q.; Huang, Y.; Chen, Z.; Wu, J. Individual tree crown delineation using localized contour tree method and airborne lidar data in coniferous forests. *Int. J. Appl. Earth Obs. Geoinf.* **2016**, *52*, 82–94. [CrossRef]
17. Huang, Y.; Chen, Z.; Wu, B.; Chen, L.; Mao, W.; Zhao, F.; Wu, J.; Wu, J.; Yu, B. Estimating roof solar energy potential in the downtown area using a gpu-accelerated solar radiation model and airborne lidar data. *Remote Sens.* **2015**, *7*, 15877. [CrossRef]
18. Guo, B.; Huang, X.F.; Zhang, F.; Sohn, G.H. Classification of airborne laser scanning data using jointboost. *ISPRS-J. Photogramm. Remote Sens.* **2015**, *100*, 71–83. [CrossRef]
19. Chehata, N.; Guo, L.; Mallet, C. Airborne lidar feature selection for urban classification using random forests. *Int. Arch. Photogramm. Remote Sens.* **2009**, *38*, W8.
20. Weinmann, M.; Jutzi, B.; Hinz, S.; Mallet, C. Semantic point cloud interpretation based on optimal neighborhoods, relevant features and efficient classifiers. *ISPRS J. Photogramm. Remote Sens.* **2015**, *105*, 286–304. [CrossRef]
21. Tóvári, D. Segmentation Based Classification of Airborne Laser Scanner Data. Ph.D. Thesis, Karlsruhe Institute of Technology, Karlsruhe, Germany, 2006.
22. Darmawati, A. Utilization of Multiple Echo Information for Classification of Airborne Laser Scanning Data. Master's Thesis, ITC Enschede, Enschede, The Netherlands, 2008.
23. Yao, W.; Hinz, S.; Stilla, U. Object extraction based on 3d-segmentation of lidar data by combining mean shift with normalized cuts: Two examples from urban areas. In Proceedings of the 2009 Joint Urban Remote Sensing Event, Shanghai, China, 20–22 May 2009; pp. 1–6.
24. Yang, B.S.; Dong, Z.; Zhao, G.; Dai, W.X. Hierarchical extraction of urban objects from mobile laser scanning data. *ISPRS J. Photogramm. Remote Sens.* **2015**, *99*, 45–57. [CrossRef]
25. Xu, S.; Vosselman, G.; Elberink, S.O. Multiple-entity based classification of airborne laser scanning data in urban areas. *ISPRS J. Photogramm. Remote Sens.* **2014**, *88*, 1–15. [CrossRef]
26. Lee, I.; Schenk, T. Perceptual organization of 3d surface points. *Int. Arch. Photogramm. Remote Sens.* **2002**, *34*, 193–198.
27. Filin, S.; Pfeifer, N. Neighborhood systems for airborne laser data. *Photogramm. Eng. Remote Sens.* **2005**, *71*, 743–755. [CrossRef]
28. Linsen, L.; Prautzsch, H. Local versus global triangulations. In Proceedings of the Eurographics'01, Manchester, UK, 5–7 September 2001.
29. Mitra, N.J.; Nguyen, A. Estimating surface normals in noisy point cloud data. In Proceedings of the Nineteenth Annual Symposium on Computational Geometry, San Diego, CA, USA, 8–10 June 2003; pp. 322–328.
30. Lalonde, J.-F.; Unnikrishnan, R.; Vandapel, N.; Hebert, M. Scale selection for classification of point-sampled 3D surfaces. In Proceedings of the Fifth International Conference on 3-D Digital Imaging and Modeling (3DIM'05), Ottawa, ON, Canada, 13–16 June 2005; pp. 285–292.
31. Pauly, M.; Keiser, R.; Gross, M. Multi-scale feature extraction on point-sampled surfaces. *Comput. Graph. Forum* **2003**, *22*, 281–289. [CrossRef]
32. Belton, D.; Lichti, D.D. Classification and segmentation of terrestrial laser scanner point clouds using local variance information. *Int. Arch. Photogramm. Remote Sens.* **2006**, *36*, 44–49.
33. Demantke, J.; Mallet, C.; David, N.; Vallet, B. Dimensionality based scale selection in 3d lidar point clouds. *Int. Arch. Photogramm. Remote Sens.* **2011**, *38*, W12. [CrossRef]

34. Weinmann, M.; Jutzi, B.; Mallet, C. Semantic 3d scene interpretation: A framework combining optimal neighborhood size selection with relevant features. *ISPRS Ann. Photogramm. Remote Sens. Spat. Inf. Sci.* **2014**, *2*, 181–188. [CrossRef]
35. Wang, Y.; Cheng, L.; Chen, Y.M.; Wu, Y.; Li, M.C. Building point detection from vehicle-borne lidar data based on voxel group and horizontal hollow analysis. *Remote Sens.* **2016**, *8*, 419. [CrossRef]
36. Zhang, J.X.; Lin, X.G.; Ning, X.G. Svm-based classification of segmented airborne lidar point clouds in urban areas. *Remote Sens.* **2013**, *5*, 3749–3775. [CrossRef]
37. Vo, A.V.; Linh, T.H.; Laefer, D.F.; Bertolotto, M. Octree-based region growing for point cloud segmentation. *ISPRS-J. Photogramm. Remote Sens.* **2015**, *104*, 88–100. [CrossRef]
38. Guan, H.; Yu, J.; Li, J.; Luo, L. Random forests-based feature selection for land-use classification using lidar data and orthoimagery. *Int. Arch. Photogramm. Remote Sens.* **2012**, *39*, B7. [CrossRef]
39. Johnson, A.E.; Hebert, M. Using spin images for efficient object recognition in cluttered 3d scenes. *IEEE Trans. Pattern Anal. Mach. Intell.* **1999**, *21*, 433–449. [CrossRef]
40. Osada, R.; Funkhouser, T.; Chazelle, B.; Dobkin, D. Shape distributions. *ACM Trans. Graph.* **2002**, *21*, 807–832. [CrossRef]
41. Rusu, R.B.; Blodow, N.; Beetz, M. Fast point feature histograms (FPFH) for 3d registration. In Proceedings of the IEEE International Conference on Robotics and Automation (ICRA'09), Kobe, Japan, 12–17 May 2009; pp. 3212–3217.
42. Rusu, R.B.; Marton, Z.C.; Blodow, N.; Beetz, M. Persistent point feature histograms for 3d point clouds. In Proceedings of the 10th International Conference on Intelligent Autonomous Systems (IAS-10), Baden-Baden, Germany, 23–25 July 2008; pp. 119–128.
43. Tombari, F.; Salti, S.; Di Stefano, L. Unique signatures of histograms for local surface description. In Proceedings of the European Conference on Computer Vision, Heraklion, Crete, Greece, 5–11 September 2010; pp. 356–369.
44. Guan, H.Y.; Li, J.; Chapman, M.; Deng, F.; Ji, Z.; Yang, X. Integration of orthoimagery and lidar data for object-based urban thematic mapping using random forests. *Int. J. Remote Sens.* **2013**, *34*, 5166–5186. [CrossRef]
45. Lodha, S.K.; Kreps, E.J.; Helmbold, D.P.; Fitzpatrick, D.N. Aerial lidar data classification using support vector machines (svm). In Proceedings of the Third International Symposium on 3D Data Processing, Visualization, and Transmission, Chapel Hill, NC, USA, 14–16 June 2006; pp. 567–574.
46. Lodha, S.K.; Fitzpatrick, D.M.; Helmbold, D.P. Aerial lidar data classification using adaboost. In Proceedings of the Sixth International Conference on 3-D Digital Imaging and Modeling, Montreal, QC, Canada, 21–23 August 2007; pp. 435–442.
47. Lodha, S.K.; Fitzpatrick, D.M.; Helmbold, D.P. Aerial lidar data classification using expectation-maximization. *Proc. SPIE* **2007**. [CrossRef]
48. Kim, H.; Sohn, G. 3d classification of power-line scene from airborne laser scanning data using random forests. *Int. Arch. Photogramm. Remote Sens* **2010**, *38*, 126–132.
49. Kim, H.; Sohn, G. Random forests based multiple classifier system for power-line scene classification. *ISPRS Int. Arch. Photogramm., Remote Sens. Spat. Inf. Sci.* **2011**, 253–258. [CrossRef]
50. Breiman, L. Random forests. *Mach. Learn.* **2001**, *45*, 5–32. [CrossRef]
51. Belgiu, M.; Dragut, L. Random forest in remote sensing: A review of applications and future directions. *ISPRS J. Photogramm. Remote Sens.* **2016**, *114*, 24–31. [CrossRef]
52. Diaz-Uriarte, R.; de Andres, S.A. Gene selection and classification of microarray data using random forest. *BMC Bioinform.* **2006**, *7*, 3. [CrossRef] [PubMed]
53. Xu, B.; Jiang, W.; Shan, J.; Zhang, J.; Li, L. Investigation on the weighted ransac approaches for building roof plane segmentation from lidar point clouds. *Remote Sens.* **2016**, *8*, 5. [CrossRef]
54. Vosselman, G.; Klein, R. Visualisation and structuring of point clouds. In *Airborne and Terrestrial Laser Scanning*; Whittles Publishing: Dunbeath, UK, 2010; pp. 43–79.
55. Lin, Y.; Wang, C.; Cheng, J.; Chen, B.; Jia, F.; Chen, Z.; Li, J. Line segment extraction for large scale unorganized point clouds. *ISPRS J. Photogramm. Remote Sens.* **2015**, *102*, 172–183. [CrossRef]
56. Ni, H.; Lin, X.; Ning, X.; Zhang, J. Edge detection and feature line tracing in 3d-point clouds by analyzing geometric properties of neighborhoods. *Remote Sens.* **2016**, *8*, 710. [CrossRef]

57. Rabbani, T.; van den Heuvel, F.; Vosselmann, G. Segmentation of point clouds using smoothness constraint. *Int. Arch. Photogramm. Remote Sens.* **2006**, *36*, 248–253.
58. Arsigny, V.; Fillard, P.; Pennec, X.; Ayache, N. Log-euclidean metrics for fast and simple calculus on diffusion tensors. *Magn. Reson. Med.* **2006**, *56*, 411–421. [CrossRef] [PubMed]
59. Chen, C.; Liaw, A.; Breiman, L. *Using Random Forest to learn Imbalanced Data*; University of California, Berkeley: Berkeley, CA, USA, 2004; pp. 1–12.
60. Strobl, C.; Boulesteix, A.L.; Augustin, T. Unbiased split selection for classification trees based on the gini index. *Comput. Stat. Data Anal.* **2007**, *52*, 483–501. [CrossRef]
61. Lin, X.; Zhang, J. Segmentation-based filtering of airborne lidar point clouds by progressive densification of terrain segments. *Remote Sens.* **2014**, *6*, 1294. [CrossRef]
62. He, Y. Automated 3D Building Modelling from Airborne Lidar Data. Ph.D. Thesis, University of Melbourne, Melbourne, Victoria, Australia, 2015.
63. PCL-The Point Cloud Library, 2012. Available online: http://pointclouds.org/ (accessed on 11 September 2014).
64. Libsvm, 2014. Available online: http://www.csie.ntu.edu.tw/~cjlin/libsvm (accessed on 25 March 2015).
65. 2008 Iowa River Flood Lidar, Iowa City, and the Clear Creek Watershed. Available online: http://opentopo.sdsc.edu/lidarDataset?opentopoID=OTLAS.012012.26915.1 (accessed on 21 January 2016).
66. Umd-NASA Carbon Mapping/Sonoma County Vegetation Mapping and LiDAR Program. Available online: http://opentopo.sdsc.edu/datasetMetadata?otCollectionID=OT.092014.2871.1 (accessed on 21 January 2016).